

# Towards Instance-Wise Calibration: Local Amortized Diagnostics and Reshaping of Conditional Densities (LADaR)

Biprateep Dey<sup>1,2,3,4,5,6</sup>, David Zhao<sup>7</sup>, Brett H. Andrews<sup>1,2</sup>, Jeffrey A. Newman<sup>1,2</sup>, Rafael Izbicki<sup>8</sup> and Ann B. Lee<sup>7</sup>

<sup>1</sup>Department of Physics and Astronomy, University of Pittsburgh

<sup>2</sup>Pittsburgh Particle Physics, Astrophysics, and Cosmology Center (PITT PACC), University of Pittsburgh

<sup>3</sup>Department of Statistical Sciences, University of Toronto

<sup>4</sup>Canadian Institute for Theoretical Astrophysics (CITA), University of Toronto

<sup>5</sup>Dunlap Institute for Astronomy & Astrophysics, University of Toronto

<sup>6</sup>Vector Institute

<sup>7</sup>Department of Statistics and Data Science, Carnegie Mellon University

<sup>8</sup>Department of Statistics, Federal University of São Carlos (UFSCar)

**Abstract.** There is a growing interest in conditional density estimation and generative modeling of a target  $y$  given complex inputs  $\mathbf{x}$ . However, off-the-shelf methods often lack instance-wise calibration — that is, for individual inputs  $\mathbf{x}$ , the individual estimated probabilities can be very different from the true probabilities, even when the estimates are reasonable when averaged over the entire population. This paper introduces the LADaR (Local Amortized Diagnostics and Reshaping of Conditional Densities) framework and proposes an algorithm called Cal-PIT, which produces interpretable local calibration diagnostics and includes a mechanism to recalibrate the initial model.

Our Cal-PIT algorithm learns a single local probability–probability map from calibration data to assess and quantify where corrections are needed across the feature space. When necessary, it reshapes the initial distribution into an estimate with approximate instance-wise calibration. We illustrate the LADaR framework by applying Cal-PIT to synthetic examples, including probabilistic forecasting with sequences of images as inputs, akin to predicting the wind speed of tropical cyclones from satellite imagery. Our main science application is conditional density estimation of galaxy distances given imaging data (so-called photometric redshift estimation). On a benchmark photometric redshift data challenge, Cal-PIT achieves better conditional density estimation (as measured by the conditional density estimation loss) than all 11 other literature methods tested. This demonstrates its potential for meeting the stringent photometric redshift requirements for next generation weak gravitational lensing analyses.<sup>†</sup>

*Keywords:* Conditional Density Estimation, Local Coverage Diagnostics, Optimal Transport Map, Calibrated Distributions, Reliable Uncertainty Quantification, Posterior Approximations.

<sup>†</sup> Code available as a Python package here: <https://github.com/lee-group-cmu/Cal-PIT>

## 1. Introduction

In recent decades, many scientific fields have progressed from computing point predictions (or a single best guess of a quantity of interest) to developing *conditional density estimates (CDEs) and generative models* of a response/“target” variable  $Y \in \mathbb{R}$  given covariates/features  $\mathbf{X} \in \mathbb{R}^d$ . This paradigm shift is evident in various disciplines, such as in astrophysics (e.g., Mandelbaum et al. 2008; Malz & Hogg 2022), in weather forecasting (e.g., Gneiting 2008; Ravuri et al. 2021; Li et al. 2024), in financial risk management (e.g., Timmermann 2000), and in epidemiological projections (e.g., Alkema et al. 2007).

The paradigm shift has been driven by two main factors. First, advances in measurement technology across engineering, physical, and biological sciences are producing data with unprecedented depth, richness, and scope. To fully exploit these data in downstream analyses, we need precise estimates of the uncertainty in a response variable  $Y$  given observable data  $\mathbf{X}$  (see Section 1.2 for two applications from the physical sciences that motivated this work). Second, we are experiencing a rapid growth of high-capacity machine learning algorithms that allow for uncertainty quantification of complex, high-dimensional data of different modalities. Two examples of such datasets come from (1) large astronomical surveys that collect images and spectroscopic data for tens of millions of stars, galaxies and other astrophysical objects (York et al., 2000; Gaia Collaboration et al., 2016; Dey et al., 2019; DESI Collaboration et al., 2022) and (2) earth-observing satellites for environmental and climate science (see, e.g., NASA’s Earth Observing System<sup>†</sup> and next-generation Earth System Observatory,<sup>‡</sup>). For the latter, the dimension  $d$  of the input space (representing, e.g., the number of image pixels or different spatial locations) is usually several orders of magnitude larger than  $10^6$ . In addition to enabling uncertainty quantification for complex inputs, modern machine learning methods allow us to “amortize” the computation; that is, to perform the compute-intensive training process only once, which allows for very fast inference and scaling to massive data sets.

In terms of methods for uncertainty quantification (UQ), we have an ever expanding list of approaches:

- *Explicit conditional density estimation (CDE) methods*, which directly estimate probability density functions  $f(y|\mathbf{x})$  via, e.g., mixture density networks (MDN; Bishop 1994), kernel mixture networks (Ambrogioni et al., 2017), Bayesian neural networks (see, e.g., Goan & Fookes 2020 and references therein), normalizing flows including neural autoregressive models (Papamakarios et al., 2019; Kobyzev et al., 2021), Gaussian process CDEs (Dutordoir et al., 2018), or simpler nonparametric CDE methods (Izbicki & Lee, 2016, 2017; Dalmaso et al., 2020);
- *Implicit CDE methods and generative models*, which encode the conditional distribution implicitly, e.g., variational autoencoders (VAEs; Kingma & Welling

<sup>†</sup> <https://eosps.nasa.gov/>

<sup>‡</sup> <https://science.nasa.gov/earth-science/missions/earth-system-observatory/>

2013), conditional generative adversarial networks (cGANs; Mirza & Osindero 2014), diffusion models (Sohl-Dickstein et al., 2015; Ho et al., 2020; Nichol & Dhariwal, 2021; Dhariwal & Nichol, 2021; Ho & Salimans, 2022) and transformer-based generative models (Vaswani et al., 2017; Radford et al., 2019);

- *Quantile regression* methods that estimate all conditional quantiles simultaneously (Chung et al., 2021a; Fasiolo et al., 2021; Tagasovska & Lopez-Paz, 2019; Amerise, 2018; Liu & Wu, 2011; Feldman et al., 2021; Lim et al., 2021).
- *Dropout and other ensemble techniques*, which estimate the uncertainty about  $y$  by generating multiple predictions using different models (Gal & Ghahramani, 2016; Lakshminarayanan et al., 2017; Rahaman et al., 2021).

The goal of this paper is not to add to this list, but rather to provide trustworthy uncertainty quantification in a predictive setting. We address two main concerns: (i) whether one can trust the output of a model that provides the uncertainty in  $y$  given  $\mathbf{x}$ , and (ii) how to improve an initial conditional density estimate or generative model when it cannot be trusted.

### 1.1. Trustworthy Uncertainty Quantification

*The importance of local (or instance-wise) calibration.* CDEs can lead to misleading conclusions in a predictive setting, if the estimated distribution does not approximately satisfy *local or instance-wise* calibration (Equation 1) with the estimated conditional distribution  $\hat{F}(y|\mathbf{x})$  (with density function  $\hat{f}(y|\mathbf{x})$ ) being approximately the same as the true distribution  $F(y|\mathbf{x})$  for all  $y \in \mathbb{R}$  and all  $\mathbf{x} \in \mathcal{X}$ . That is, local calibration means that the predicted conditional probability of occurrence of an event matches its true probability for *every* value of  $\mathbf{x}$ , and not just on average (or marginally) over the entire population of  $\mathbf{x}$ .

Instance-wise UQ is essential in many practical applications; e.g., in astrophysical studies, for predicting the physical properties of individual galaxies from measured fluxes; in weather forecasts, for predicting the probability of rainfall based on current environmental conditions; and in medical research, for estimating a drug’s efficacy for individuals of specific demographics.

Achieving instance-wise calibration can also be essential to algorithmic fairness as it prevents over- or under-prediction of risks for certain groups (Kleinberg et al., 2016; Zhao et al., 2020). Finally, from locally calibrated CDEs, one can also derive prediction bands for  $Y$  that do not under-/over-cover certain instances (see Remark 2 and Equation 7 on the relationship between calibrated CDEs and calibrated prediction sets).

*Unfortunately, off-the-shelf CDE methods can be very far from being calibrated.* The main reason is that CDEs and quantile regression methods are typically fitted by minimizing a loss function that does not directly depend upon calibration. Popular loss functions include, e.g, the Kullback-Leibler (KL) divergence (Kullback & Leibler, 1951), integral probability metrics (Papamakarios et al., 2019; Dalmaso et al., 2020), and the pinball loss (Koenker & Hallock, 2001). As noted by, e.g., Guo et al. (2017)

and Chung et al. (2021b, Proposition 1), modern machine learning methods tend to unequally favor prediction accuracy and sharpness over calibration. Different solutions have been proposed to address this issue for specific problems, including introducing new loss functions that trade off sharpness and calibration (Chung et al., 2021b), and loss functions that enforce independence of sharpness and coverage (Feldman et al., 2021).

*Local versus marginal calibration.* A further challenge in obtaining local calibration (aside from merely developing a loss function that ensures instance-level uncertainty quantification) is that most metrics that assess the calibration of CDEs — such as the widely adopted probability integral transform (PIT; Gan & Koehler 1990) and simulator-based calibration (SBC; Talts et al. 2018) — consider a weaker notion of calibration such as *average or marginal calibration* (Equation 2), where one assesses coverage of CDEs on average over all  $\mathbf{x}$ ’s instead of for every  $\mathbf{x}$ . In fact, average calibration is often simply referred to as just “calibration” (see, e.g., Gneiting & Katzfuss 2014; Kuleshov et al. 2018). However, as noted by, for example, Schmidt et al. (2020), the PIT statistic is a flawed metric as it can be optimal even if  $\hat{F}(y|\mathbf{x}) = F(y)$ ; i.e., when the estimated conditional distribution completely ignores the input  $\mathbf{x}$ . More generally, inconsistencies in various regions of the feature space can cancel out to produce optimal results when viewed as an ensemble (Zhao et al., 2021; Jitkrittum et al., 2020a; Luo et al., 2021). For instance, Zhao et al. (2021, Theorem 1) showed that a good estimator of  $F(y|g(\mathbf{x}))$ , where  $g(\mathbf{x})$  is any function, will pass tests that only assess marginal coverage. In particular, even if  $\hat{F}$  did not use relevant features, its estimates would still be (marginally) calibrated.

## 1.2. Well-Calibrated CDEs are Essential for the Physical Sciences

Our work on calibration of CDEs is motivated by two main applications in astronomy and weather forecasting:

(i) *Photometric redshift estimation of galaxies.* Redshift ( $z$ ) is a measurable proxy for distances to other galaxies and is crucial for studies of astrophysics and cosmology. Direct measurement of redshift via spectroscopy is however not feasible for the very large number of galaxies for which we have images. Redshift estimates are hence often predicted from less resource-intensive imaging data, resulting in measurements called photometric redshifts or photo- $z$ ’s.

Some downstream applications of photo- $z$  estimates require extremely reliable uncertainty quantification. Forthcoming large data sets from multi-billion dollar imaging experiments such as the Rubin Observatory’s Legacy Survey of Space and Time (LSST; Ivezić et al. 2019), the Nancy Grace Roman Space Telescope (Akeson et al., 2019), and the Euclid Mission (Laureijs et al., 2011) will crucially depend on photo- $z$ ’s to achieve their scientific objectives. The requirements of these projects on the accuracy of photo- $z$  CDEs are extremely strict: errors in the moments of redshift distributions for samples used to measure cosmological parameters must be within approximately 0.1% of the truth to ensure that downstream physical analyses are not degraded (The LSST Dark

Energy Science Collaboration et al., 2018).

In this paper, we choose calibration of CDEs of galaxy photometric redshift (as detailed in Section 4) as our main application. This choice is motivated by the significant potential impact that improved photo- $z$  estimates can have on the physical sciences, and the existence of well-established benchmarks for photo- $z$  estimation methods, provided by the LSST-Dark Energy Science Collaboration’s Photo- $z$  data challenge (Schmidt et al., 2020).

(ii) *Probabilistic forecasting of tropical cyclone (TC) intensity from satellite imagery.* Tropical cyclones are highly organized, rotating storms that are among the most costly natural disasters in the United States. TC intensity forecasts have improved in recent years, but these improvements have been relatively slow during the last decade compared to improvements in track forecasts, particularly at 24-hour lead times (DeMaria et al., 2014). The latest generation of geostationary satellites (GOES), such as GOES-16, now provides unprecedented spatio-temporal resolution of TC structure and evolution (Schmit et al., 2017). A broad array of recent works involving neural networks has explored the wealth of information of GOES imagery for TC short-term intensity prediction (e.g., Olander et al. 2021; Griffin et al. 2022), but so far statistical forecasting techniques still struggle with producing ensemble or probabilistic forecasts that reliably quantify uncertainty in the predictions.

In Section 3.2, we present a synthetic example that highlights the efficacy of our method in diagnosing and recalibrating intensity forecasts based on high-dimensional sequence data, specifically data of the same form as TC GOES imagery. Note that unlike photo- $z$  estimates — which are already used by a very large astronomy community — data-driven CDEs based on entire image sequences have not yet been employed in TC operational forecasts. We have therefore chosen to illustrate our approach of local amortized diagnostics and reshaping of densities on a synthetic example where we can easily assess performance using Monte Carlo (MC) sampling, with the anticipation that these techniques will be useful later for probabilistic models fitted to actual TC intensities and observed satellite imagery.

### 1.3. Our Contribution

To ensure trustworthy uncertainty quantification of conditional densities, it is essential to have (i) interpretable diagnostics that can assess instance-wise calibration and failure modes of an initial model across the entire feature space, and (ii) computationally efficient methods that can reshape CDEs so that they are approximately calibrated for every  $\mathbf{x}$ . The initial model can, for example, represent the best approximation to the true conditional density in a restricted family of functions defined by, e.g, physics-motivated and interpretable models, or models limited to a set of easily accessible input features.

The goal is to morph the initial model toward the true distribution of observed data with a nonparametric correction, when such a correction is needed. This work offers two primary contributions:

- From a methodological perspective, we present a unified framework for interpretable diagnostics and reshaping of entire CDEs through a single Probability-Probability (P-P) map learned from calibration data,  $\mathcal{D} = \{(\mathbf{X}_1, Y_1), \dots, (\mathbf{X}_n, Y_n)\}$ , that implicitly encodes the true distribution  $F(y|\mathbf{x})$ . Our approach is fully “amortized,” which means that once a regression model (Equation 3) is trained to learn the mapping, no additional training is required for new data. We refer to the general framework of Local Amortized Diagnostics and Reshaping of CDEs as LADaR, and call our proposed algorithm Cal-PIT. The first prototype code of Cal-PIT occurred in (Dey et al., 2021); the full ready-to-use and modifiable implementation is now available as a Python package at <https://github.com/lee-group-cmu/Cal-PIT>.
- From an application perspective, Cal-PIT is uniquely positioned to provide diagnostics and ensure that photo- $z$  CDEs are *locally* calibrated (i.e., not only as a full ensemble), which will be necessary for the astrophysics community to meet the stringent photo- $z$  requirements for next generation-astronomical surveys. Figure 8 and Table 1 demonstrate the full potential of Cal-PIT applied to a key benchmark photo- $z$  data set, where Cal-PIT outperforms the current state-of-the-art for diagnostics and estimation of photo- $z$  CDEs. Crucially, Cal-PIT can (i) accurately reshape biased probability distributions and (ii) reshape unimodal distributions into multimodal distributions—both common failure modes for common photo- $z$  estimation methods. Furthermore, Cal-PIT has the flexibility to be used with *high-dimensional* and *dependent sequence* data. Section 3.2 shows Cal-PIT applied to probabilistic forecasting with sequences of images as inputs, akin to predicting the wind speed of tropical cyclones (TCs) from satellite imagery.

## 2. Methodology

*Objective and notation.* Our LADaR goal is to reshape an initial (often simple) cumulative distribution  $\hat{F}(y|\mathbf{x})$ , or equivalently, its conditional density  $\hat{f}(y|\mathbf{x})$ , to achieve approximate instance-wise calibration with respect to some implicit (often more complex but not explicitly known) target distribution  $F(y|\mathbf{x})$ . Instance-wise calibration is defined as

$$\hat{F}(y|\mathbf{x}) = F(y|\mathbf{x}), \quad \text{for all } y, \text{ at every } \mathbf{x}, \quad (1)$$

and is sometimes also referred to as conditional or local calibration. Instance-wise or conditional calibration implies marginal calibration

$$\hat{F}(y) = F(y), \quad \text{for all } y, \quad (2)$$

whereas the reverse implication is not true.

To achieve instance-wise calibration, we assume the availability of i.i.d. calibration data  $\mathcal{D} = \{(\mathbf{X}_1, Y_1), \dots, (\mathbf{X}_n, Y_n)\}$  from  $F_{\mathbf{X},Y}(\mathbf{x}, y)$ , the joint distribution of  $(\mathbf{X}, Y)$ , where  $\mathbf{x} \in \mathcal{X} \subseteq \mathbb{R}^d$  and  $y \in \mathcal{Y} \subseteq \mathbb{R}$ . We assume that the joint distribution is a product  $F_{\mathbf{X},Y}(\mathbf{x}, y) = F(y|\mathbf{x})F(\mathbf{x})$  of the target distribution  $F(y|\mathbf{x})$  and some sampling distribution  $F(\mathbf{x})$  with support over the entire feature space  $\mathcal{X}$ .



In this paper, we propose a solution to the problem of diagnosing and ensuring local calibration of conditional densities based on probability integral transforms. We refer to the algorithm and the code as **Cal-PIT**. The details are as follows.

### 2.1. Overview of the *Cal-PIT* Algorithm

The **Cal-PIT** algorithm first computes interpretable diagnostics using regression that identifies the failure modes of the initial conditional density model and pinpoints the location of poorly calibrated instances in a potentially high-dimensional feature space. The same regression function used for diagnostics is then used to continuously transform the potentially misspecified CDE into a new CDE that is approximately calibrated for all  $\mathbf{x}$ .

**Cal-PIT** builds on the observation that an estimate of a cumulative distribution function (CDF),  $\hat{F}$ , is calibrated for every instance  $\mathbf{x}$ , if and only if its probability integral transform (PIT) value conditional on  $\mathbf{x}$ , defined by  $\text{PIT}(Y; \mathbf{X}) := \hat{F}(Y|\mathbf{X})$  is uniformly distributed (Zhao et al., 2021, Corollary 1). As a result, if a CDE is well-calibrated, the cumulative distribution function of the PIT (hereafter PIT-CDF), defined as the cumulative distribution of the PIT random variable evaluated at  $\gamma \in (0, 1)$ ,

$$r^{\hat{F}}(\gamma; \mathbf{x}) := \mathbb{P}(\text{PIT}(Y; \mathbf{X}) \leq \gamma \mid \mathbf{x}), \quad (3)$$

will be approximately  $\gamma$  for all  $\mathbf{x} \in \mathcal{X}$  and  $\gamma \in (0, 1)$ . In other words, the PIT-CDF will then correspond to the CDF of a uniform random variable for all  $\mathbf{x}$ . The PIT-CDF provides valuable insight as to whether  $\hat{F}$  is miscalibrated, and if so, for what instances  $\mathbf{x}$ , for what type of deviations, and to what extent. Specifically, local probability-probability (P-P) plots — which graph the PIT-CDF value  $r^{\hat{F}}(\gamma; \mathbf{x})$ , the empirical probability, against  $\gamma$ , the theoretically expected probability, for fixed  $\mathbf{x}$  — offer valuable information as to how close the probability distribution  $\hat{F}(Y|\mathbf{X})$  is to  $F(Y|\mathbf{X})$  at different locations  $X = \mathbf{x}$  in the feature space. Figure 1 shows a schematic diagram of some P-P plots and how to interpret them; Appendix E describes a Monte Carlo procedure for quantifying statistical significance of a local deviation in terms of p-values and confidence sets.

However, in practice, the PIT-CDF is unknown. Section 2.2 describes how one can estimate the PIT-CDF across the feature space from calibration data using a regression method suitable for the problem at hand. Our proposed approach is *amortized*, in the sense that one can train on  $\mathbf{x}$  and  $\gamma$  jointly, after which the function PIT-CDF can be evaluated for any new values of  $\mathbf{x}$  and  $\gamma$ . Finally, Section 2.3 describes how the learnt PIT-CDF itself defines a push-forward map (Equation 5) that reshapes the densities so as to achieve approximate local calibration. Algorithm 1 summarizes the details of the **Cal-PIT** method.

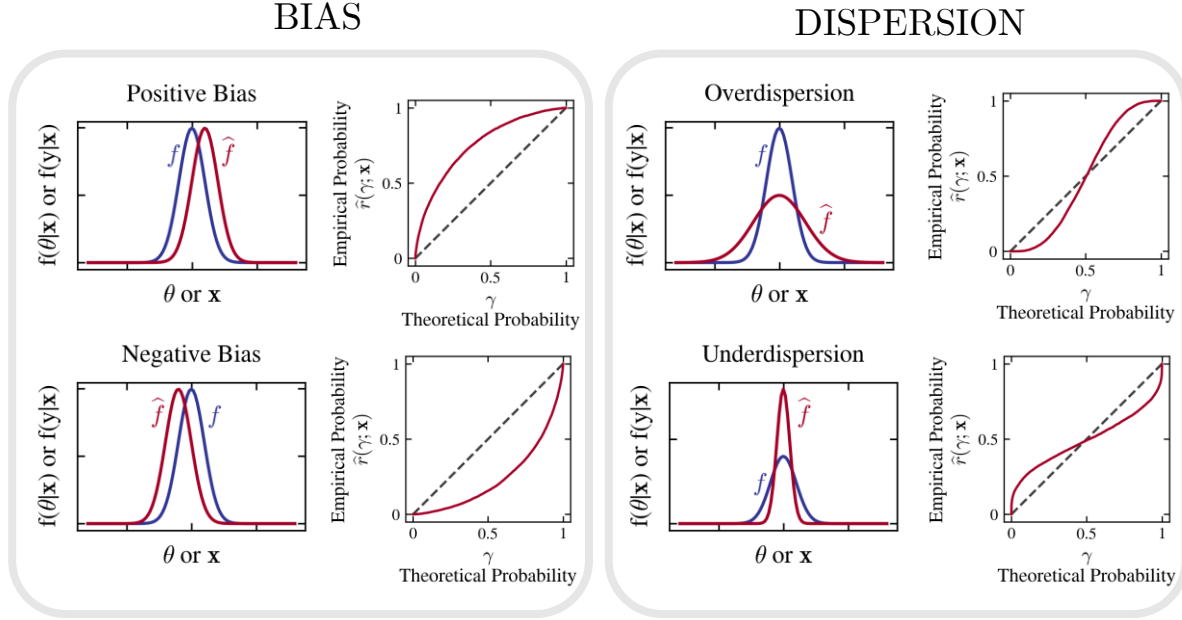


Figure 1: **Interpretable diagnostics.** P-P plots are commonly used to assess how well a probability density model fits actual data. Such plots display, in a clear and interpretable way, effects like *bias* (left panel) and *dispersion* (right panel) in an estimated distribution  $\hat{f}$  vis-a-vis the true data-generating distribution  $f$ . Our framework yields an amortized approach to constructing local P-P plots for comparing Bayesian posteriors  $\hat{f}(\theta|\mathbf{x})$  or predictive densities  $\hat{f}(y|\mathbf{x})$  at *any* location  $\mathbf{x}$  of the feature space  $\mathcal{X}$ . Figure adapted from Zhao et al. 2021. An interactive version of this figure can be found at: [https://lee-group-cmu.github.io/cal-pit-paper/fig\\_1\\_interactive/](https://lee-group-cmu.github.io/cal-pit-paper/fig_1_interactive/).

## 2.2. Estimating the PIT-CDF

We observe that the PIT-CDF in Equation 3 is the regression (conditional mean) of a binary random variable  $W^\gamma := \mathbb{I}(\text{PIT}(Y; \mathbf{X}) < \gamma)$  on  $\mathbf{X}$ ; that is,

$$r^{\hat{f}}(\gamma; \mathbf{x}) = \mathbb{E}[W^\gamma | \mathbf{x}], \quad (4)$$

where the expectation  $\mathbb{E}[\cdot | \mathbf{x}]$  denotes an average with respect to the (unknown) target distribution  $F(y|\mathbf{x})$ . The above expression indicates that we can estimate the PIT-CDF across the entire feature space  $\mathcal{X}$ , as well as for different quantiles  $\gamma \in (0,1)$ , via regression methods.

**Cal-PIT** is implemented as follows: First, we augment the calibration data  $\mathcal{D}$  by drawing multiple quantile values  $\gamma_{i,1}, \dots, \gamma_{i,K} \sim U(0,1)$  for each calibration data point ( $i = 1, \dots, n$ ) and some chosen hyperparameter  $K$ . Next, we define the random variable

$$W_{i,j} := \mathbb{I}(\text{PIT}(Y_i; \mathbf{X}_i) \leq \gamma_{i,j}).$$

Finally, we train a suitable regression method using the augmented calibration sample  $\mathcal{D}' = \{(\mathbf{X}_i, \gamma_{i,j}, W_{i,j})\}_{i,j}$  to predict  $W_{i,j}$  with  $(\mathbf{X}_i, \gamma_{i,j})$  as inputs, for  $i = 1, \dots, n$  and  $j = 1, \dots, K$ . The computed regression function is an estimate of  $\mathbb{P}(\text{PIT}(Y; \mathbf{X}) \leq \gamma | \mathbf{x})$ . Since  $r^{\hat{f}}(\gamma; \mathbf{x})$  is a non-decreasing function of  $\gamma$ , we typically choose monotonic neural



networks (Wehenkel & Louppe, 2019) minimizing the binary cross entropy loss (Good, 1952) as our regression method, especially for applications with complex and high-dimensional inputs of different modality.

### 2.3. Reshaping Conditional Densities by Mapping Probabilities to Probabilities

Cal-PIT uses the estimated PIT-CDF to reshape the initial CDE  $\hat{f}$  into a new CDE  $\tilde{f}$  that is approximately locally consistent across the *entire* feature space. Figure 2 illustrates the equivalence of Cal-PIT to optimal transport maps (Santambrogio, 2015).

Our procedure for morphing one probability density into a new “recalibrated” density works as follows: Consider a fixed evaluation point  $\mathbf{x}$  and any  $y_0 \in \mathcal{Y}$ . Let  $\gamma := \hat{F}(y_0|\mathbf{x})$ . If the regression is perfectly estimated (that is,  $\hat{r}^{\hat{f}} = r^{\hat{f}}$ ), then, as long as both  $F$  and  $\hat{F}$  are continuous and  $\hat{F}$  dominates  $F$  (see Assumptions 2 and 3 in Appendix F for details), it holds that

$$r^{\hat{f}}(\gamma; \mathbf{x}) := \mathbb{P}\left(\hat{F}(Y|\mathbf{x}) \leq \gamma \mid \mathbf{x}\right) = \mathbb{P}(Y \leq y_0 \mid \mathbf{x}) = F(y_0|\mathbf{x}).$$

In other words, the regression function  $r^{\hat{f}}$  changes the initial CDE so that the probability of observing the response variable  $Y$  below  $y_0$  is now indeed  $F(y_0|\mathbf{x})$  rather than  $\hat{F}(y_0|\mathbf{x})$ ; this mapping of probabilities to probabilities is illustrated by the right panel of figure 2.

It follows directly that for fixed  $\hat{F}$ ,

$$r^{\hat{f}}\left(\hat{F}(y|\mathbf{x}); \mathbf{x}\right) = \mathbb{P}\left(\hat{F}(Y|\mathbf{x}) \leq \hat{F}(y|\mathbf{x}) \mid \mathbf{x}\right) = \mathbb{P}(Y \leq y \mid \mathbf{x}) = F(y|\mathbf{x})$$

The above result suggests that we can use the estimated regression,  $\hat{r}^{\hat{f}}$ , which is an approximation of the PIT-CDF,  $r^{\hat{f}}$ , to transform the original distribution  $\hat{F}$  with density  $\hat{f}$  into a new “recalibrated” conditional distribution  $\tilde{F}$  with density  $\tilde{f}$ :

**Definition 1** (Recalibrated CDE). *The recalibrated CDE of  $Y$  given  $\mathbf{x}$  is defined through the  $P$ - $P$  map,*

$$\tilde{F}(y|\mathbf{x}) := \hat{r}^{\hat{f}}\left(\hat{F}(y|\mathbf{x}); \mathbf{x}\right), \quad (5)$$

where  $\hat{r}^{\hat{f}}$  is the regression estimator of the PIT-CDF (Equation 3).

If the PIT-CDF is well-estimated, then the new CDE will achieve instance-wise calibration. The next theorem shows that, under some assumptions, we can directly relate the quality of the recalibration (or how close the “recalibrated” distribution is to the target distribution in a mean-squared-error sense) to the mean-squared-error of the regression estimator:

**Theorem 1** (Performance of the recalibrated CDE). *Under Assumptions 2, 3 and 4 (Appendix F),*

$$\mathbb{E}\left[\int \int \left(\tilde{F}(y|\mathbf{x}) - F(y|\mathbf{x})\right)^2 dP(y, \mathbf{x})\right] = K \mathbb{E}\left[\int \int \left(\hat{r}^{\hat{f}}(\gamma; \mathbf{x}) - r^{\hat{f}}(\gamma; \mathbf{x})\right)^2 d\gamma dP(\mathbf{x})\right],$$

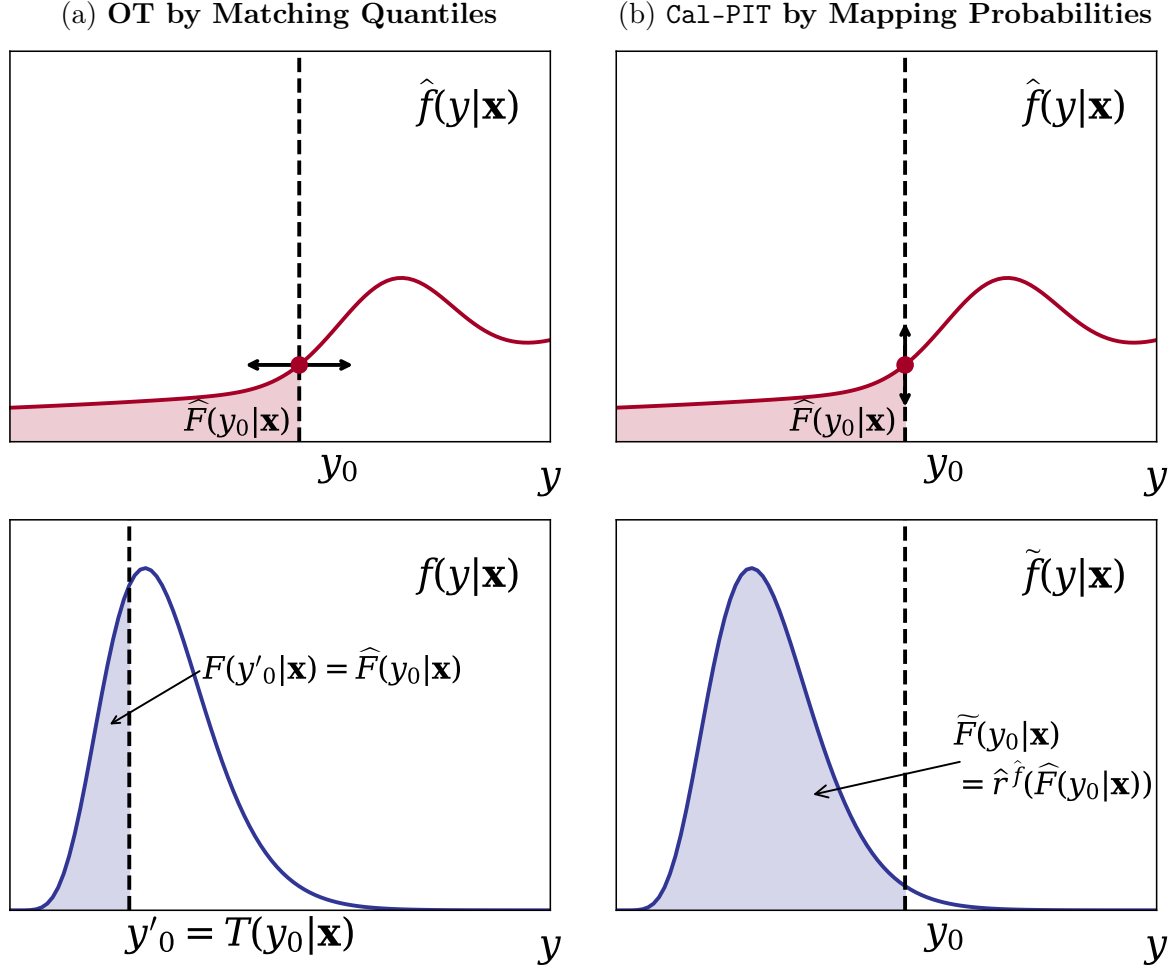


Figure 2: Cal-PIT is an algorithmic solution to an optimal transport problem. *Left (a):* The optimal transport (OT) map from  $\hat{F}(y|\mathbf{x})$  to  $F(y|\mathbf{x})$  uses quantile matching for fixed  $\mathbf{x}$  to match calibration data, where the OT map is given by  $T(y_0|\mathbf{x}) := F^{-1}(\hat{F}(y_0|\mathbf{x}) | \mathbf{x})$ . The OT map rearranges one PDF into another. In practice, however, the true target distribution  $F$  is not known and off-the-shelf conditional distributions are usually far from being even marginally calibrated. *Right (b):* Cal-PIT constructs an estimate of the entire conditional distribution  $F(y|\mathbf{x})$  by mapping probabilities, yielding the recalibrated distribution (Equation 5)  $\tilde{F}(y_0|\mathbf{x}) := \hat{r}^{\hat{f}}(\hat{F}(y_0|\mathbf{x}); \mathbf{x})$ , and hence an estimate of the OT map through  $\hat{T}(y_0|\mathbf{x}) := \tilde{F}^{-1}(\hat{F}(y_0|\mathbf{x}) | \mathbf{x})$  for every  $\mathbf{x} \in \mathcal{X}$  and  $y_0 \in \mathcal{Y}$  (Equation 13). That is, the P-P map reshapes the original PDF, but the end result is the same, as illustrated by the side-by-side panels. Thus, Cal-PIT, which is based on P-P maps, can be seen as a computationally efficient means to estimating the entire family of OT maps across a potentially high-dimensional feature space via a *single* regression that directly targets instance-wise calibration. See Section 5 and Appendix C for further details.

The rate of convergence of  $\tilde{F}(y|\mathbf{x})$  to the target distribution  $F(y|\mathbf{x})$  is given by Corollary 1.

Algorithm 1 details the Cal-PIT procedure for computing the PIT-CDF from calibration data, and for constructing recalibrated CDEs and prediction intervals. In practice, for each  $\mathbf{x}$  of interest, we first evaluate  $\tilde{F}(y|\mathbf{x})$  across a grid  $G$  of  $y$ -values, and

**Algorithm 1** Cal-PIT

**Require:** initial CDE  $\hat{f}(y|\mathbf{x})$  evaluated at  $y \in G$ ; calibration set  $\mathcal{D} = \{(\mathbf{X}_1, Y_1), \dots, (\mathbf{X}_n, Y_n)\}$ ; oversampling factor  $K$ ; evaluation points  $\mathcal{V} \subset \mathcal{X}$ ; nominal miscoverage level  $\alpha$ , flag HPD (true if computing HPD sets)

**Ensure:** new distribution  $\tilde{F}(y|\mathbf{x})$ , Cal-PIT interval  $C(\mathbf{x})$ , new density estimate  $\tilde{f}(y|\mathbf{x})$ , for all  $\mathbf{x} \in \mathcal{V}$

---

```

1: // Learn PIT-CDF from augmented and upsampled calibration data  $\mathcal{D}'$ 
2: Set  $\mathcal{D}' \leftarrow \emptyset$ 
3: for  $i$  in  $\{1, \dots, n\}$  do
4:   for  $j$  in  $\{1, \dots, K\}$  do
5:     Draw  $\gamma_{i,j} \sim U(0, 1)$ 
6:     Compute  $W_{i,j} \leftarrow \mathbb{I}(\text{PIT}(Y_i; \mathbf{X}_i) \leq \gamma_{i,j})$ 
7:     Let  $\mathcal{D}' \leftarrow \mathcal{D}' \cup \{(\mathbf{X}_i, \gamma_{i,j}, W_{i,j})\}$ 
8:   end for
9: end for
10: Use  $\mathcal{D}'$  to learn  $\hat{r}^{\hat{f}}(\gamma; \mathbf{x}) := \hat{\mathbb{P}}(\text{PIT}(Y; \mathbf{x}) \leq \gamma \mid \mathbf{x})$  via a regression of  $W$  on  $\mathbf{X}$  and  $\gamma$ ,
    which is monotonic w.r.t.  $\gamma$ .
11:
12: // Map initial CDE into a new CDE by applying learnt PIT-CDF
13: for  $\mathbf{x} \in \mathcal{V}$  do
14:   // Construct recalibrated CDE
15:   Compute  $\hat{F}(y|\mathbf{x}) \leftarrow \text{cumsum}(\hat{f}(y|\mathbf{x}))$  for  $y \in G$ 
16:   Let  $\tilde{F}(y|\mathbf{x}) \leftarrow \hat{r}^{\hat{f}}(\hat{F}(y|\mathbf{x}); \mathbf{x})$  for  $y \in G$ 
17:   Apply interpolating (or smoothing) splines to obtain  $\tilde{F}(\cdot|\mathbf{x})$  and  $\tilde{F}^{-1}(\cdot|\mathbf{x})$ 
18:   Differentiate  $\tilde{F}(y|\mathbf{x})$  to obtain new distribution  $\tilde{f}(y|\mathbf{x})$  for  $y \in G$ 
19:   Renormalize  $\tilde{f}(y|\mathbf{x})$  according to Izbicki & Lee \(2016, Section 2.2\)
20:
21:   // Construct Cal-PIT interval with conditional coverage  $1 - \alpha$ 
22:   Compute  $C(\mathbf{x}) \leftarrow [\tilde{F}^{-1}(0.5\alpha|\mathbf{x}); \tilde{F}^{-1}(1 - 0.5\alpha|\mathbf{x})]$ .
23:   if HPD then
24:     Obtain HPD sets  $C(\mathbf{x}) = \{y : \tilde{f}(y|\mathbf{x}) \geq \tilde{t}_{\mathbf{x},\alpha}\}$ , where  $\tilde{t}_{\mathbf{x},\alpha}$  is such that
        $\int_{y \in C_{\alpha}(\mathbf{x})} \tilde{f}(y|\mathbf{x}) dy = 1 - \alpha$ 
25:   end if
26: end for
27: return  $\tilde{F}(y|\mathbf{x})$ ,  $C(\mathbf{x})$ ,  $\tilde{f}(y|\mathbf{x})$ , for all  $\mathbf{x} \in \mathcal{V}$ 

```

---

then use linear or spline-based interpolation scheme to calculate the derivatives to finally obtain  $\tilde{f}(y|\mathbf{x})$ , our estimate of the recalibrated CDE at  $\mathbf{x}$ .

**Remark 1.** If the initial model is good, then  $r$  is easy to estimate; for instance,  $\hat{f} = f$  implies a constant function  $r^{\hat{f}}(\gamma; \mathbf{x}) = \gamma$ . However,  $\hat{f}$  needs to have support on the entire

range of the target variable  $y$  across the feature space  $\mathcal{X}$ . Depending on the application, a viable initial model could, for example, be an estimate of the marginal distribution  $f(y)$ , a uniform distribution with finite support (as in Experiment 2 of [Appendix A](#), Example 3), an initial fit of the density with a Gaussian distribution (as in the TC application in Section 3.2), or a nonparametric density estimate (as in Experiment 1 of [Appendix A](#), Example 3). In the photo- $z$  application in Section 4, we use a weighted sum of the marginal distribution  $f(y)$  and a Gaussian model for  $f(y|\mathbf{x})$ . The Gaussian model was obtained from a widely popular photo- $z$  method (GP $z$ ; [Almosallam et al. 2016](#)); the marginal distribution was then added to expand the support of the fitted Gaussian distribution.

**Remark 2** (CDEs and Prediction Sets). As a by-product of conditional distributions, one can derive various quantities of interest, such as moments, kurtosis, prediction intervals, or even more general prediction bands; such as Highest Predictive Density (HPD) regions  $\{y : f(y|\mathbf{x}) > c\}$ , where  $f$  is the conditional density associated to  $F$ ; see [Appendix D](#) for details on how to compute HPD regions. By construction, locally calibrated CDEs yield prediction bands with approximately correct conditional coverage. That is, suppose that  $C_\alpha(\mathbf{X})$  is a  $(1 - \alpha)/100\%$  prediction band derived from the CDF  $\hat{F}$ . Local calibration of  $\hat{F}$  then implies that the prediction bands  $C_\alpha(\mathbf{X})$  have approximate nominal coverage

$$\mathbb{P}(Y \in C_\alpha(\mathbf{X}) | \mathbf{X} = \mathbf{x}) = 1 - \alpha, \quad (6)$$

for every instance  $\mathbf{x} \in \mathcal{X}$ . On the other hand, it is difficult to convert prediction bands and quantile estimates to entire CDEs without additional assumptions. That is, calibrated CDEs imply calibrated prediction bands but not vice versa. For example, Theorem 3 in [Appendix F](#) shows that a Cal-PIT prediction interval at  $\mathbf{x}$ , defined as

$$C_\alpha(\mathbf{x}) := \left[ \tilde{F}^{-1}(0.5\alpha|\mathbf{x}), \tilde{F}^{-1}(1 - 0.5\alpha|\mathbf{x}) \right], \quad (7)$$

achieves asymptotic conditional coverage, even if the initial CDE  $\hat{f}(y|\mathbf{x})$  is not consistent.

### 3. Synthetic Examples

#### 3.1. Example 1: Diagnostics and Reshaping of CDEs via P-P maps

This example illustrates the LADaR framework with Cal-PIT: We start with an initial model  $f_0(y|\mathbf{x})$  (in this case, a Gaussian density with correct mean and fixed variance). Then, via a PIT-CDF regression (Equation 4), we learn the local diagnostics which can be visualized via P-P plots similar to Figure 1. Finally, we reshape the initial densities to better fit the calibration data by applying the same learned P-P map (that is, the PIT-CDF transformation) to the initial densities (Equation 5).

As an illustration, we create two data settings: “skewed” and “kurtotic”. The data are drawn from the family of sinh-arcsinh normal distributions ([Jones & Pewsey, 2009, 2019](#)), where the *skewed* data follow

$$Y_A | X \sim \text{sinh-arcsinh}(\mu = X, \sigma = 2 - |X|, \gamma = X, \tau = 1),$$

and the *kurtotic* data follow

$$Y_B|X \sim \sinh\text{-arcsinh}(\mu = X, \sigma = 2, \gamma = 0, \tau = 1 - X/4).$$

In each setting, we start with an initial Gaussian model given by

$$Y|X \sim \mathcal{N}(\mu = X, \sigma = 2),$$

and we learn the PIT-CDF function  $\hat{r}^{f_0}(\gamma; \mathbf{x})$  from a calibration set of  $n = 10000$  pairs of  $(X, Y)$ .

The top panel of figure 3 shows “Local Amortized Diagnostics” for the skewed setting: The first row graphs a *local discrepancy score* (LDS) across the feature space (see Kodra et al. 2023 for an example use of the global analog), where the LDS is defined as

$$D(\mathbf{x}) := \frac{1}{|G|} \sum_{\gamma \in G} (\hat{r}^{f_0}(\gamma; \mathbf{x}) - \gamma)^2, \quad (8)$$

for a set  $G \subset [0, 1]$  of  $\gamma$  values. The LDS is a one-number summary that estimates the amount of discrepancy between the initial model and the true density in terms of coverage: a large value of  $D(\mathbf{x})$  indicates that  $f_0$  is miscalibrated at the evaluation point  $\mathbf{x}$ . The PIT-CDF function  $\hat{r}^{f_0}$  then provides more detailed information on *how* the initial model  $f_0(y|\mathbf{x})$  might deviate from the true density  $f(y|\mathbf{x})$  at  $\mathbf{x}$ , as illustrated by the shape of the P-P plots in the second row. The same PIT-CDF function  $\hat{r}^{f_0}$  also provides us with an approximation of the entire *optimal transport map* from  $f_0(y|\mathbf{x})$  to  $f(y|\mathbf{x})$  at any  $\mathbf{x}$ . Top panel II (“Reshaping of Densities”) shows examples of morphing of the initial density  $f_0$  (blue) into an approximation  $\tilde{f}$  (red) of the final density defined by Equation 13. For illustrative purposes, we show intermediate curves  $s\tilde{f} + (1-s)f_0$  for a few different values  $s \in [0, 1]$ .

Finally, because we know the true data-generating distribution  $F$ , we can directly assess the quality of the reshaped densities  $\tilde{f}$  by first generating MC samples from the true distribution at each evaluation point  $\mathbf{x}$ , and then computing a local version of the *continuous ranked probability score* (CRPS). More specifically: CRPS is a proper scoring rule commonly used to evaluate probabilistic predictions (Matheson & Winkler, 1976). The local CRPS loss at a point  $(\mathbf{x}, y)$  is typically defined as

$$L_{\text{CRPS}}(\tilde{f}; \mathbf{x}, y) = \int_{-\infty}^{\infty} \left( \tilde{F}(t|\mathbf{x}) - \mathbb{I}(y \leq t) \right)^2 dt, \quad (9)$$

which checks whether a single draw  $y \sim F(Y|\mathbf{x})$  (from the unknown true distribution  $F$ ) is consistent with the estimated distribution  $\tilde{F}(y|\mathbf{x})$ . For our synthetic examples, we are however able to generate an entire MC sample  $Y_1, \dots, Y_B \sim F(y|\mathbf{x})$  (from the known true distribution  $F$ ) at *any* fixed evaluation point  $\mathbf{x}$  for some chosen large value  $B$ . We then define the local Monte Carlo CRPS (MC-CRPS) loss at fixed  $\mathbf{x}$  as

$$L_{\text{MC-CRPS}}(\tilde{f}; \mathbf{x}, f) = \int \left( \tilde{F}(Y < t|\mathbf{x}) - \frac{1}{B} \sum_{b=1}^B I(Y_b < t) \right)^2 dt, \quad (10)$$

For large  $B$ , Equation 10 is close to zero when  $\tilde{F}(\cdot|\mathbf{x})$  is a good estimate of  $F(\cdot|\mathbf{x})$ . Furthermore, Equation 10 is, up to a constant that does not depend on  $\tilde{F}$ , approximately the same as  $\mathbb{E} \left[ L_{\text{CRPS}}(\tilde{f}; \mathbf{x}, Y) \mid \mathbf{x} \right]$ , the conditional mean of the CRPS loss given  $\mathbf{X} = \mathbf{x}$  (see ?? for details). The bottom panel of Figure 3 shows the local MC-CRPS results before and after applying Cal-PIT. Figure 4 showcases the LADaR approach and results for the “kurtotic” setting.



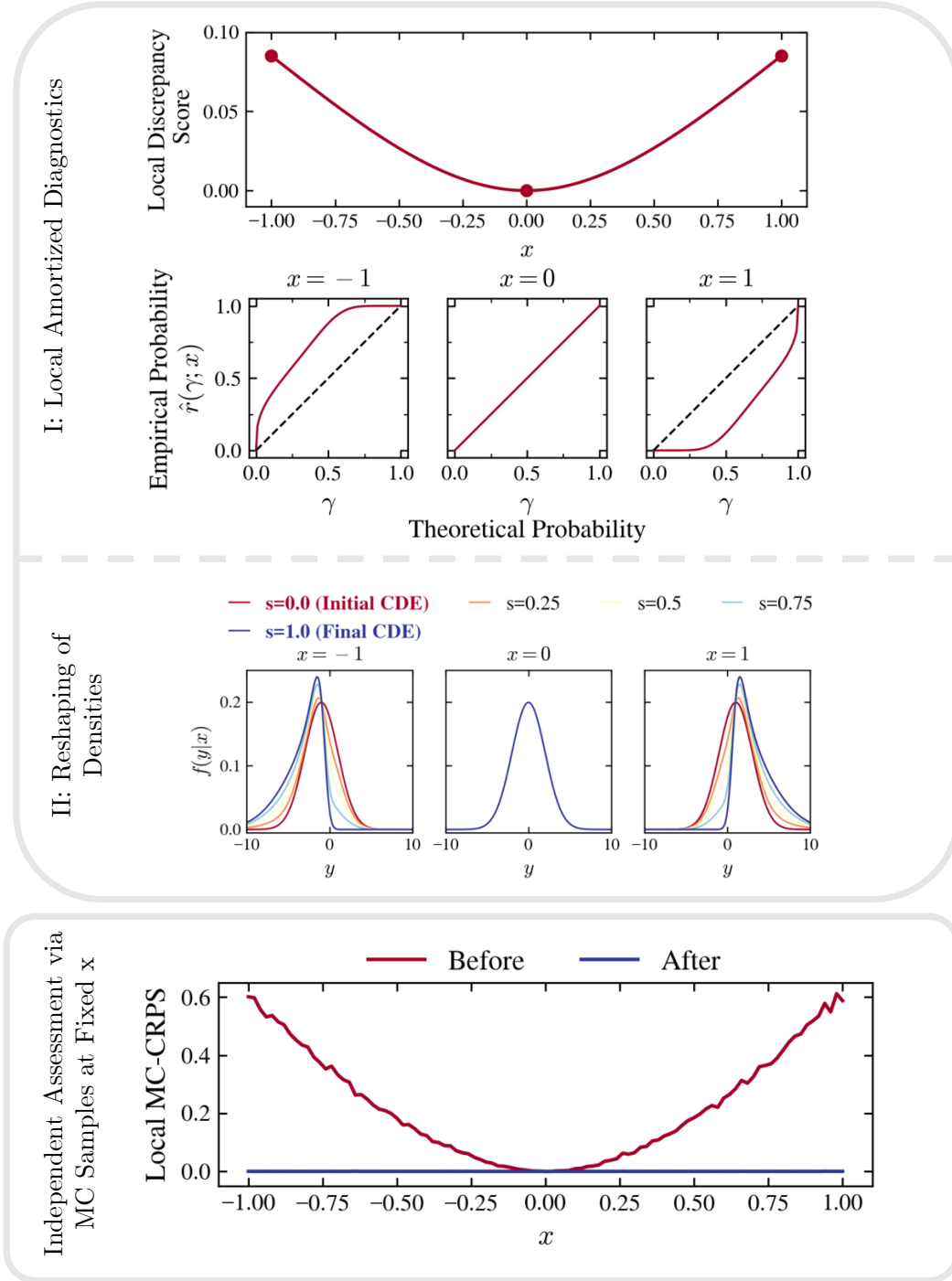


Figure 3: **Illustration of LADaR framework: Example 1 skewed data.** Initial CDE is Gaussian, but the true distribution is skewed. *Top panel (I)*: Local discrepancy score across the input space (first row) and examples of diagnostic P-P plots (second row). Cal-PIT identifies that the model is *positively/negatively biased* relative to calibration data at  $X = -1$  /  $X = 1$  but well-estimated at  $X = 0$ . The diagnostics define a family of P-P maps for reshaping the initial densities to fit the calibration data across the feature space. *Top panel (II)*: Continuous morphing of densities via Cal-PIT, illustrated at the three evaluation points, from the initial Gaussian distributions (red;  $s = 0$ ) to the final distributions (blue;  $s = 1$ ). For illustrative purposes, we have included intermediate values of  $s$  to show the morphing of distributions. *Bottom panel*: Independent assessment of final results by computing a local Monte Carlo version of the continuous ranked probability score (MC-CRPS) at fixed  $x$  before and after Cal-PIT.

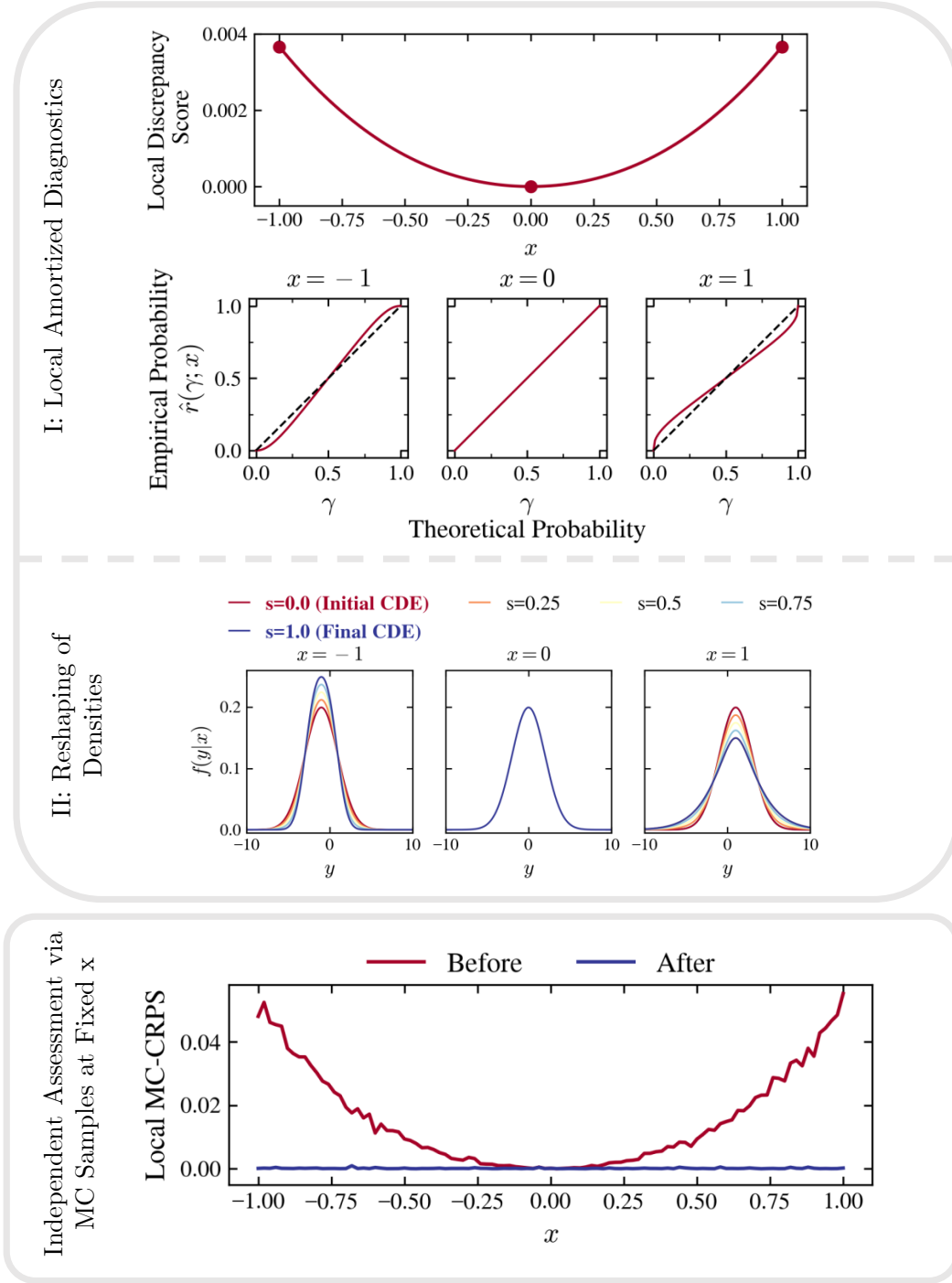


Figure 4: **Illustration of LADaR framework: Example 1 kurtotic data.** Initial CDE is Gaussian, but the true distribution is kurtotic. *Top panel I:* Local discrepancy score across the input space (first row) and examples of diagnostic P-P plots (second row). Cal-PIT identifies that the model is *over-/under-dispersed* relative to calibration data at  $X = -1$  /  $X = 1$  but well-estimated at  $X = 0$ . The diagnostics define a family of P-P maps for reshaping the initial densities so as to fit the calibration data across the feature space. *Top panel II:* Continuous morphing of densities via Cal-PIT, illustrated at the three evaluation points, from the initial Gaussian distributions (red;  $s = 0$ ) to the final distributions (blue;  $s = 1$ ). For illustrative purposes, we have included intermediate values of  $s$  to show the morphing of distributions. *Bottom panel:* Independent assessment of final results by computing a local Monte Carlo version of the continuous ranked probability score (MC-CRPS) at fixed  $x$  before and after Cal-PIT.

### 3.2. Example 2: Probabilistic Nowcasting with High-Dimensional Sequence Data as Inputs

Our next synthetic example is motivated by tropical cyclone (TC) intensity forecasting using satellite image data. This application is challenging both because of the high-dimensional nature of spatio-temporal satellite data and because the observations are correlated in time. Figure 5, right, shows an example of a 24-hour sequence  $\mathbf{S}_{<t}$  of consecutive radial profiles (one-dimensional functions) extracted from Geostationary Operational Environmental Satellite (GOES) infrared imagery (Janowiak et al., 2020).

Infrared (IR) imagery as observed by GOES measures the cloud-top temperature, which is a proxy for the strength of convection (the key component of the mechanism through which TCs extract energy from the ocean). Hence, each computed sequence  $\mathbf{S}_{<t}$  can be seen as a summary of the spatio-temporal evolution of TC convective structure leading up to time  $t$ , where patterns in  $\mathbf{S}_{<t}$  signaling strengthening/weakening convection are predictors of intensifying/weakening storms; that is, they predict changes in TC intensities,  $I_\tau$ , for  $\tau \geq t$ .

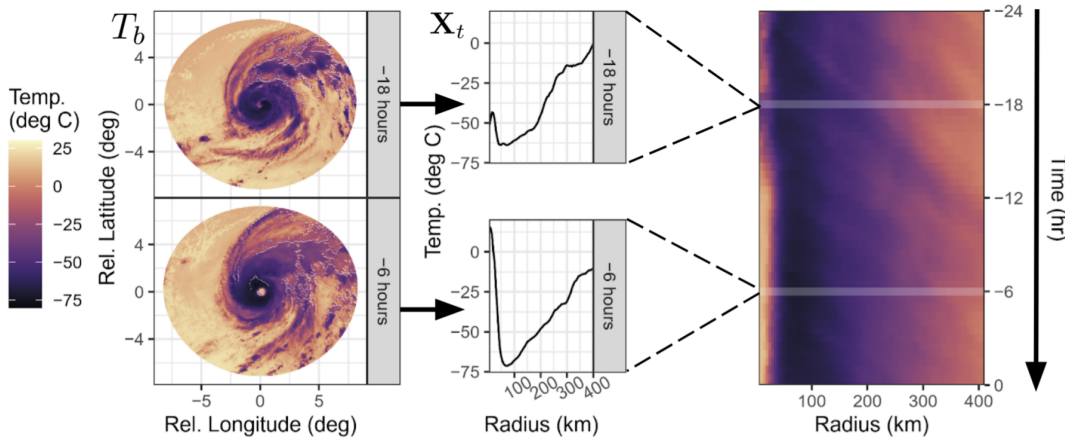


Figure 5: **TC satellite images.** *Left:* A sequence of TC-centered cloud-top temperature images from GOES. *Center:* We represent each GOES image with a radial profile of azimuthally-averaged cloud-top temperatures. *Right:* The 24-hour sequence of consecutive radial profiles, sampled every 30 minutes, defines a structural trajectory  $\mathbf{S}_{<t}$  or Hovmöller diagram. Figure adapted from McNeely et al. (2022).

As a proof of concept of our LADaR framework, we create a synthetic example with the same format as actual TC data. The details are described in supplementary material S3†. Figure 6 shows an example of a simulated storm. On the left, we have a toy Hovmöller diagram of the evolution of “convective structure”  $\{(\mathbf{X}_t)\}_{t \geq 0}$ , with each row representing the radial profile  $\mathbf{X}_t \in \mathbb{R}^{120}$  of temperature as a function of radial distance from the storm center; time evolution is top-down in hours. On the right, we have  $\{Y_t\}_{t \geq 0}$ , the simulated “TC intensities” at corresponding times  $t$ . The trajectory  $\mathbf{S}_{<t} := (\mathbf{X}_{t-47}, \mathbf{X}_{t-46}, \dots, \mathbf{X}_t)$  represents the 24-hour history of convective structure (48 radial profiles). We simulate 800 “storms” according to a fitted TC length distribution.

† Supplementary Materials: [https://lee-group-cmu.github.io/cal-pit-paper/supplementary\\_material.pdf](https://lee-group-cmu.github.io/cal-pit-paper/supplementary_material.pdf)

Sequence data  $\{(\mathbf{S}_{<t}, Y_t)\}$  from the same storm are shifted by 30 minutes; hence, they are strongly correlated. Sequence data from different storms, on the other hand, are independent.

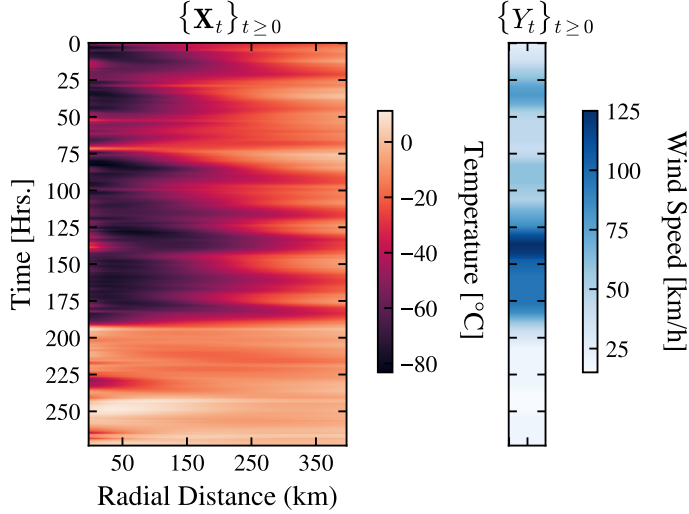


Figure 6: **Synthetic data in Example 2.** Simulated radial profiles  $\{\mathbf{X}_t\}_{t \geq 0}$  and intensities  $\{Y_t\}_{t \geq 0}$  for an example TC. *Left:* Each row represents the radial profile  $\mathbf{X}_t$  of temperature as a function of radial distance from the storm center at time  $t$ . Our predictors are 48-hour overlapping sequences  $\{\mathbf{S}_t\}_{t \geq 0}$  with data from the same “storm” being highly dependent. *Right:* The target response, here shown as a time series  $\{Y_t\}_{t \geq 0}$  of simulated TC intensities.

Our goal is to “nowcast” the conditional distribution  $Y_t|\mathbf{S}_{<t}$ , where  $Y_t$  is the intensity at time  $t$ . Here we illustrate how Cal-PIT can diagnose and improve upon an initial convolutional mixture density network (ConvMDN) model. In our example, we perform training, calibration, and testing on different simulated “storms”: First, we fit an initial CDE (ConvMDN; D’Isanto & Polsterer 2018), which estimates  $f(y|\mathbf{s})$  as a unimodal Gaussian, based on a train set with 8000 points,  $\{(\mathbf{S}_{<t}, Y_t)\}$  (see supplementary material S3 for details). Next, we apply Cal-PIT to learn  $\hat{r}^{\hat{f}}(\gamma; \mathbf{s})$  using 8000 calibration points. (Note that the data within the same storm are highly dependent; hence, the effective train or calibration sample sizes are much smaller than the nominal values.) Because we have access to the data-generating distribution, we can assess the performance of CDEs before and after reshaping densities by MC samples at 4000 test points.

Figure 7 summarizes the results. With the LADaR framework (top panel), we are able to identify the regions in a high-dimensional space of sequence data where our initial CDE of  $Y_t|\mathbf{S}_{<t}$  is a poor fit. In the top left panel, each point corresponds to a 24-hour structural trajectory  $\mathbf{S}_{<t}$  or sequence of radial profiles visualized in a dimensionality reduced space using principal component analysis (PCA); the points are color-coded by the local discrepancy score (LDS) between the initial model and the true distribution of calibration data according to Cal-PIT. Three specific examples of input sequences are also shown. After applying the estimated P-P map via Cal-PIT to all CDEs, we obtain near instance-wise calibration according to an independent MC assessment (bottom panel).

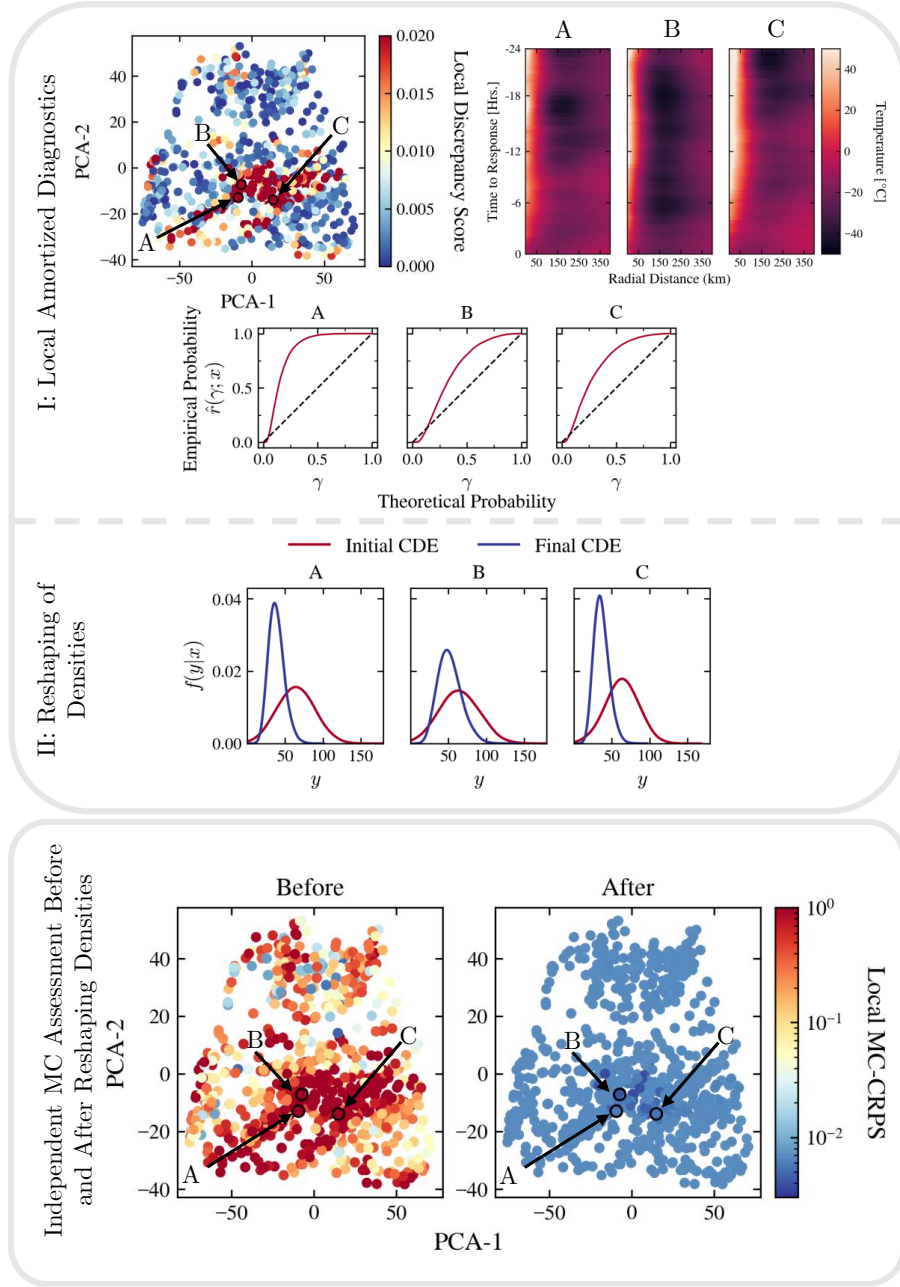


Figure 7: **Example 2: Probabilistic nowcasting with high-dimensional sequence data as inputs.** *Top panel I: Local Amortized Diagnostics.* First row: Two-dimensional PCA map of sequence data. One point in the map represents a 24-h structural trajectory  $\mathbf{S}_{<t}$  or sequence of radial profiles; the points are color-coded by the local discrepancy score (LDS) between the initial model and calibration data according to Cal-PIT. Points A–C represent three examples of inputs  $\mathbf{S}_{<t}$  where the initial model appears to perform the worst (i.e., high LDS). Second row: P–P plots help reveal the nature of the discrepancy; the initial model appears positively biased and overdispersed at the three locations. *Top panel II: Reshaping of densities.* The density of  $Y_t|\mathbf{S}_{<t}$  before (red) and after (blue) applying the P–P map. *Bottom panel: Independent MC assessment.* For synthetic data, we can compute the continuous ranked probability score (CRPS) locally for simulated MC samples at fixed  $\mathbf{S}_{<t}$ . The local Monte Carlo CRPS scores are shown before (left) and after (right) reshaping the densities. After applying the P–P map, the CDEs are well-calibrated for all inputs  $\mathbf{S}_{<t}$ .

### 3.3. Example 3: Prediction Sets

The novelty of our method lies in the fact that we can construct full CDEs with approximate instance-wise coverage. Nevertheless, as a by-product, we can also construct prediction sets with approximate conditional coverage. Given the wealth of prior literature on prediction sets, we have added an additional synthetic example in [Appendix A](#) to demonstrate that prediction sets derived from Cal-PIT are competitive with sets from conformal inference and quantile regression.

## 4. Main Application: Reshaping CDEs of Galaxy Photometric Redshifts

Many astrophysical studies depend on knowing the distances to external galaxies. Geometric distances to galaxies are incredibly difficult to measure, so astrophysicists typically use the redshift of light emitted from a galaxy as a proxy for its distance, where the spectral energy distribution (the intensity of light as a function of wavelength) is shifted to longer (redder) wavelengths due to the cosmological expansion of space. Redshifts can be precisely measured using spectroscopy to identify spectral features that occur at known wavelengths, but obtaining spectroscopic redshifts is resource-intensive. A far more efficient approach is to estimate redshifts from imaging data (i.e., photo- $z$ 's), but even with measurements at several wavelengths, imaging data produces a less precise localization of these features (and hence more uncertain photo- $z$ 's) due to a much coarser wavelength binning of photons. In particular, upcoming multi-billion dollar imaging projects like the Rubin Observatory's Legacy Survey of Space and Time (LSST; [Ivezić et al. 2019](#)), the Nancy Grace Roman Space Telescope ([Akeson et al., 2019](#)), and the Euclid Mission ([Laureijs et al., 2011](#)) will make key cosmological measurements using weak gravitational lensing (see e.g., [Mandelbaum 2018](#) for an overview), a method that relies on well-calibrated photo- $z$ 's of millions of galaxies. The demands on the accuracy of photo- $z$  CDEs for these projects are extremely stringent: discrepancies in the moments of redshift distributions for samples that are instrumental in measuring cosmological parameters must be less than approximately 0.1% to prevent degradation of subsequent physical analyses ([The LSST Dark Energy Science Collaboration et al., 2018](#)).

However, calibrating photo- $z$  CDEs remains tricky because galaxies span a wide range of intrinsic properties and spectral energy distributions ([Conroy, 2013](#)), which leads to different combinations of redshift and intrinsic spectral energy distribution producing nearly identical observed imaging data. This problem is further complicated by measurement errors and the coarseness of the spectral information available from imaging data. Thus, the estimation of photo- $z$ 's is inherently probabilistic with often non-trivial (e.g., non-Gaussian or bimodal) distributions. These distributions cannot be accurately captured by point estimates or prediction sets and must be quantified using full predictive distributions ([Benítez, 2000](#); [Mandelbaum et al., 2008](#); [Malz & Hogg, 2022](#)), which Cal-PIT is uniquely suited to estimate.

Most photo- $z$  estimation methods fall into two main classes: physics-inspired



methods that find the combination of redshift and spectral energy distribution that best matches the data (e.g., [Arnouts et al. 1999](#); [Brammer et al. 2008](#)), and (ii) data-driven methods that learn a non-linear mapping between the input imaging data and redshift (e.g., [Beck et al. 2016](#); [Zhou et al. 2021](#); [Dalmasso et al. 2020](#); [Dey et al. 2022](#)). No class of method is clearly the best for all imaging data sets, with the physics-based methods typically performing better when training data are sparse and the data-driven methods typically doing better when training data densely sample parameter space. Previous studies have used global metrics to reshape probability distributions (e.g., [Bordoloi et al. 2010](#); [Euclid Collaboration et al. 2021](#); [Kodra et al. 2023](#)), including PIT-based recalibration schemes. Regardless, no method guarantees correct *local* calibration of uncertainty estimates, a more stringent requirement that is the focus of Cal-PIT.

To showcase the effectiveness of our LADaR approach, we utilize the data set from [Schmidt et al. \(2020\)](#), which has been used as a reference for assessing photo- $z$  CDE prediction techniques. This data set was developed by assigning realistic spectral energy distributions to galaxies in a dark matter-only simulation ([DeRose et al., 2019](#)) to mimic their appearance in LSST imaging data. The input features consist of logarithmic measurements of intensity of observed galaxy light (spatially-integrated across the image) in a given wavelength range (corresponding to a photometric filter) called *apparent magnitudes* and the differences between them called *colors*. Additionally, uncertainty estimates for these measurements were also provided. For the [Schmidt et al. \(2020\)](#) data challenge, the participants were given an unbiased “training set” of  $\sim 44,000$  instances (galaxies) to which they applied 11 different physics-inspired and data-driven photo- $z$  approaches. The photo- $z$  methods were then evaluated on an unseen “test set” of  $\sim 400,000$  instances (galaxies). For this exercise, the training set was perfectly representative of the test set. [Schmidt et al. \(2020\)](#) also evaluated the performance of a method that simply predicted the marginal distribution of redshifts in the training set (i.e., the same prediction for every galaxy in the data set), which they called `trainZ`. Although this naive estimate does not contain any meaningful information about the redshift of any individual galaxy, [Schmidt et al. \(2020\)](#) demonstrated that it can perform well on many commonly used metrics that check for marginal calibration.

Reassuringly, [Schmidt et al. \(2020\)](#) found that `trainZ` performed very poorly on the conditional density estimate (CDE) loss ([Izbicki & Lee, 2017](#)), a metric of conditional coverage. The CDE loss is a proper scoring technique and the *conditional* analog of the root-mean-square-error for probabilistic regression. Given an estimate  $\tilde{f}$  of  $f$ , it is defined as

$$L(f, \tilde{f}) = \int \int [f(y|\mathbf{x}) - \tilde{f}(y|\mathbf{x})]^2 dy dP(\mathbf{x}), \quad (11)$$

where  $dP(\mathbf{x})$  is the marginal distribution of features  $\mathbf{x}$ . The CDE loss cannot be evaluated directly as it depends on the unknown true density  $f(y|\mathbf{x})$ , but it can be estimated up to a constant ( $K_f$ , dependent on  $f(y|\mathbf{x})$ ) by

$$\hat{L}(f, \tilde{f}) = \mathbb{E}_{\mathbf{x}} \left[ \int \tilde{f}(y|\mathbf{x})^2 dy \right] - 2\mathbb{E}_{\mathbf{x}, y} [\tilde{f}(y|\mathbf{x})] + K_f,$$

which is sufficient for relative comparisons between methods. The CDE loss was the only conditional metric identified and tested in the [Schmidt et al. \(2020\)](#) challenge, so we use it as our main metric for the assessment of Cal-PIT in the context of photo- $z$ 's and note that Cal-PIT is independent of the CDE loss.

For a fair comparison, we adopt the same training and test sets from [Schmidt et al. \(2020\)](#) and use the former as our calibration set to learn the local PIT-CDF. Among the methods compared by [Schmidt et al. \(2020\)](#), we use the density estimates from GPz ([Almosallam et al., 2016](#)) as our initial model. GPz uses sparse Gaussian processes to estimate the CDEs. Although, GPz produces Gaussian density estimates, it is commonly recognized that photo- $z$  conditional densities can have non-Gaussian characteristics such as long tails or bimodalities. To expand the support of the initial distributions, we took a weighted sum of the marginal distribution of redshifts in the calibration set and the GPz outputs with weights 0.1 and 0.9, respectively, as our initial CDEs. We used monotonic neural networks to learn the PIT-CDF from an input feature set of one galaxy magnitude and five colors along with their measurement uncertainties. We then use the same features to diagnose and reshape the initial densities. Finally, we assess the quality of our reshaped CDEs with the CDE loss.

Figure 8 showcases how Cal-PIT is a powerful tool for diagnosing and reshaping photo- $z$  CDEs. The top row of panel I displays a subset of the test data points in two projections (left:  $u - g$  color vs.  $i$ -band magnitude; right:  $r - i$  color vs.  $z - y$  color) of feature space with the points color-coded by the local discrepancy score. Four individual galaxies are highlighted, and their diagnostic P-P plots are shown in the second row of panel I. The first P-P plot shows an instance where the initial model was good and no substantial reshaping is necessary. The second P-P plot shows an instance where the initial guess is overdispersed, whereas the third shows an instance where the initial guess was heavily biased. The last P-P plot demonstrates a case where the P-P plot has multiple steep sections, indicating that initial model failed to express a bimodal density.

Panel II shows the initial CDE (red), the reshaped CDE (blue), and the true redshift (dotted black line and cross). Cal-PIT leverages the information contained in the diagnostics (i.e., the P-P plots from panel I) to reshape the initial CDEs and even recover bimodal CDEs from unimodal input CDEs (with the true redshift being in one of the modes). Figure 8 (bottom row) provides a clear (though not statistically rigorous) demonstration that the CDEs from Cal-PIT are indeed meaningful. Since we do not know the “ground truth” distributions for this data set, we have to rely on indirect methods to assess the quality. Specifically, we use the distribution of true redshifts of other galaxies with similar imaging data. We identify those counterparts by searching for other galaxies in the test set whose magnitudes and colors (rescaled by subtracting the mean and dividing by the standard deviation for each feature) lie within a Euclidean distance of 0.5 units of our selected galaxies. Figure 8 (bottom row) shows their redshift distribution as weighted histograms, where the weights are inversely proportional to the euclidean distance to each neighbor, along with their predicted CDEs. When the CDEs are unimodal, the nearest-neighbor histograms are also unimodal with similar widths.

Even more impressively, when our inferred CDEs are bimodal, the nearest-neighbor histograms show matching bimodal distributions, indicating that not only did **Cal-PIT** correctly find the mode with the true redshift but that it also correctly identified the other redshift solution with similar imaging properties.

Finally, Table 1 shows that **Cal-PIT** achieves a lower CDE loss than any of the methods in the LSST-DESC Photo- $z$  data challenge (Schmidt et al., 2020). The values of the CDE loss for all methods except **Cal-PIT** come from Schmidt et al. (2020), whereas the value for **Cal-PIT** was obtained by running our algorithm on the same train and test sets. As expected, there is a major improvement in the value of the CDE loss (from  $-9.93$  to  $-10.80$ ) from our input distribution (i.e., **GPz**) to our **Cal-PIT**-reshaped distributions. Moreover, **Cal-PIT** outperforms all of the other photo- $z$  methods tested by (Schmidt et al., 2020), including **FlexZBoost** (Izbicki & Lee, 2017), which was designed to minimize the CDE loss. While the improvement over **FlexZBoost** is not dramatic, **Cal-PIT** guarantees proper calibration, which **FlexZBoost** does not. Because **Cal-PIT** outperforms state-of-the-art photo- $z$  prediction methods on independent metrics while ensuring proper calibration, it is perhaps the most promising method for meeting the exacting photo- $z$  requirements of next generation imaging surveys.

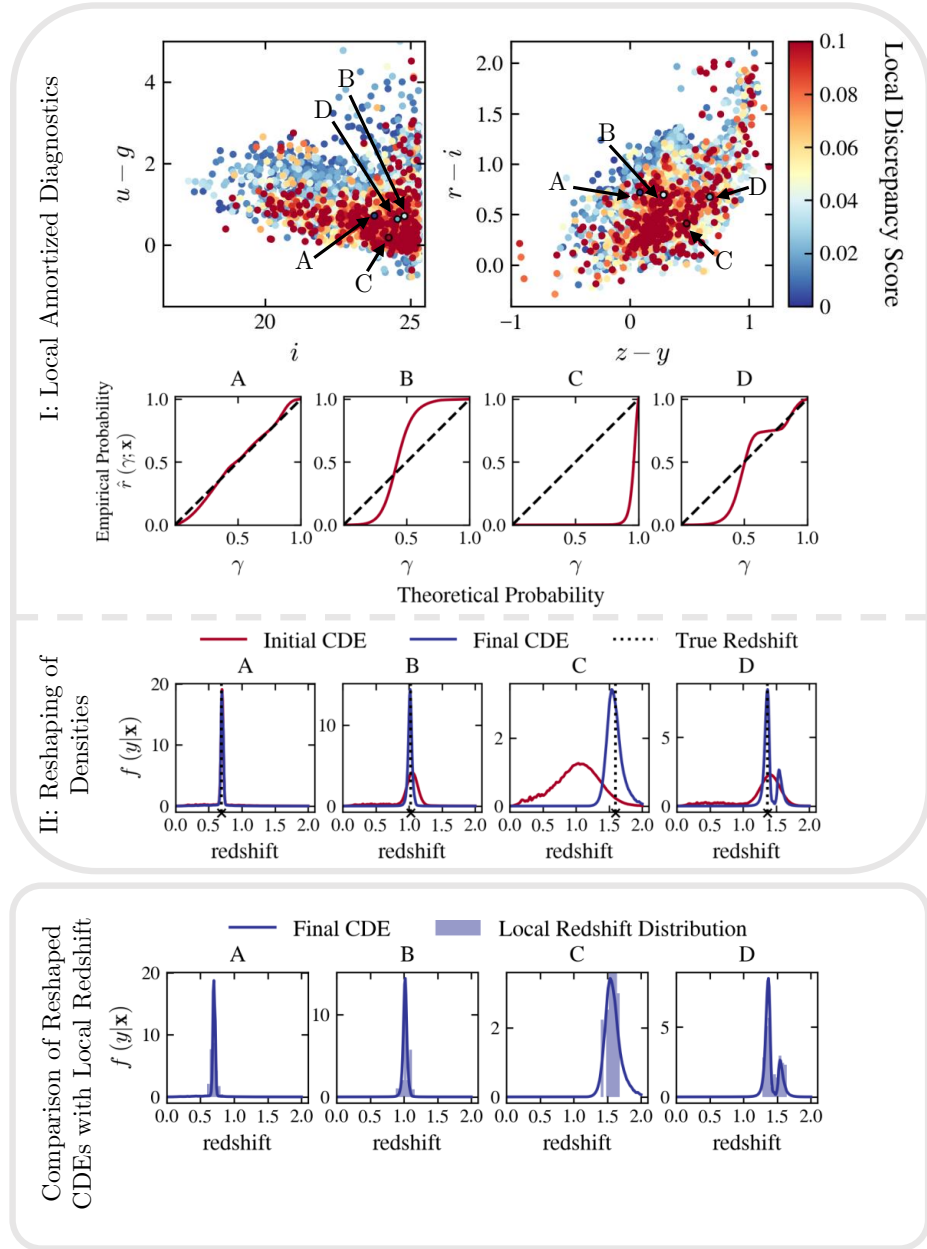


Figure 8: **Photo- $z$  application.** *Top panel I: Local amortized diagnostics.* First row: The local discrepancy score for the initial model shown in two projections of the feature space. The first figure shows galaxy  $i$ -band magnitude and  $u - g$  color space, and the second figure shows  $z - y$  color and  $r - i$  color space. The points labeled A–D correspond to the four galaxies for which we show the diagnostics and reshaping. Second row: Diagnostic P-P plots of the initial model (modified GPz CDEs; Almosallam et al. 2016) for four galaxies from the LSST-DESC Photo- $z$  Data Challenge (Schmidt et al., 2020) test set. *Top panel II: Reshaping of densities.* Photo- $z$  CDEs for the corresponding galaxies before (red) and after (blue) reshaping the densities via Cal-PIT; the true (spectroscopic) redshift is shown as a vertical dotted black line and a cross. Cal-PIT can correct for bias and over-/under-dispersion. Most impressively, it can recover accurate bimodal CDEs even if the initial estimate was unimodal. *Bottom row:* Comparison of the final reshaped CDEs (blue line) with the local “nearest-neighbor” distribution (blue shaded histogram) of true redshifts of other galaxies with similar imaging properties. Cal-PIT accurately approximates the local redshift distribution for unimodal and multimodal redshift distributions. Further, the inferred CDEs are bimodal only when the histograms are bimodal.

Table 1: Comparison of the CDE loss values for Cal-PIT and the methods benchmarked in the LSST-DESC Photo- $z$  Data Challenge (Schmidt et al., 2020). In terms of the CDE loss, Cal-PIT performs better than all of the other methods tested, including FlexZBoost, which is specifically optimized to minimize the CDE loss.

Photo- $z$ Algorithm	CDE Loss
ANNz2 (Sadeh et al., 2016)	−6.88
BPZ (Benítez, 2000)	−7.82
Delight (Leistedt & Hogg, 2017)	−8.33
EAZY (Brammer et al., 2008)	−7.07
FlexZBoost (Izbicki & Lee, 2017)	− <b>10.60</b>
GPz (Almosallam et al., 2016)	−9.93
LePhare (Arnouts et al., 1999)	−1.66
METAPhoR (Cavuoti et al., 2017)	−6.28
CMNN (Graham et al., 2018)	−10.43
SkyNet (Graff et al., 2014)	−7.89
TPZ (Carrasco Kind & Brunner, 2013)	−9.55
trainZ (Schmidt et al., 2020)	−0.83
Cal-PIT	− <b>10.80</b>

## 5. Discussion

There has been a growing interest in conditional density and generative models (see Chen et al. 2022 and references therein) — however, there are few tools for assessing whether these methods yield trustworthy (instance-wise) UQ, and there are even fewer approaches for improving conditional density models in terms of local calibration. Our proposed solution, LADaR with Cal-PIT, draws upon the success of high-capacity predictive algorithms, such as deep neural networks, to recalibrate CDEs in complex data settings with a minimum of assumptions.

Cal-PIT can assess whether an estimate  $\hat{F}(\cdot|\mathbf{x})$  is well-calibrated for all inputs  $\mathbf{x}$ , as well as correct for discrepancies. In order for Cal-PIT corrections to give good results, the initial estimate  $\hat{F}(\cdot|\mathbf{x})$  needs to place its mass on a region which is at least as large as  $F(\cdot|\mathbf{x})$  (see remark 1), but the initial fit can be poor otherwise. Good results also require calibration data to learn the regression function (Equation 3); empirically, we see that total data sizes for training and calibration are still reasonable if using the right NN architecture and training correctly. Cal-PIT does not require exchangeable data, only stationary processes; hence it can be applied to (stationary) probabilistic time series forecasting. Individually calibrated CDEs can also automatically return conditionally calibrated prediction sets. However, Cal-PIT works under the assumption that  $Y$  is continuous and does not apply to classification tasks (unlike calibration schemes in, e.g., Kull et al. 2019; Wald & Globerson 2017).

Finally, Cal-PIT can potentially be extended to multivariate output vectors  $\mathbf{Y}$  by the decomposition  $f(\mathbf{y}|\mathbf{x}) = \prod_i f(y_i|\mathbf{x}, \mathbf{y}_{<i})$ ; thus performing Cal-PIT corrections

on auto-regressive components of the conditional distribution. This is a particularly promising direction for deep autoregressive generative models (Van den Oord et al., 2016; van den Oord & Kalchbrenner, 2016; Vaswani et al., 2017; Hoogeboom et al., 2021). We are currently investigating whether Cal-PIT can improve structural forecasts for short-term tropical cyclone intensity guidance (McNeely et al., 2023). See also Linhart et al. (2022) for a multivariate extension specific to normalizing flows. Other open problems include fast sampling from recalibrated conditional distributions to generate ensemble forecasts in real time.

### 5.1. Relation to Other Methods

We conclude by discussing how Cal-PIT relates to other work in the literature.

*Goodness-of-Fit Tests and Calibration.* Goodness-of-fit of conditional density models to observed data can be assessed by two-sample tests (e.g., Andrews, 1997; Stute & Zhu, 2002; Moreira, 2003; Jitkrittum et al., 2020b). Such tests are useful for deciding whether a conditional density model needs to be improved, but do not provide any means to correct discrepancies. One way to recalibrate CDEs (proposed by, e.g., Bordoloi et al. 2010) is by first assessing how the marginal distribution of the PIT values differs from a uniform distribution by diagnostics tools (Cook et al., 2006; Freeman et al., 2017; Talts et al., 2018; D’Isanto & Polsterer, 2018), and then applying corrections to bring them into agreement. However, by construction, such recalibration schemes only improve marginal calibration. In this work, we instead build on Zhao et al. (2021), which proposes a version of PIT that is estimated across the *entire* input feature space, thereby allowing us to directly assess and target conditional coverage.

*Optimal Transport.* Cal-PIT can be thought of as a regression approach to estimating the optimal transport (see Appendix C for a review of optimal transport) that morphs a source distribution  $\hat{F}(y|\mathbf{x})$  into a target distribution  $F(y|\mathbf{x})$ . Figure 2 illustrates the parallel views of Cal-PIT and Optimal Transport (OT). The details are as follows:

Let  $Y \sim \hat{F}_{Y|\mathbf{X}}$  and  $Y' \sim F_{Y|\mathbf{X}}$  be continuous random variables with respective conditional densities  $\hat{f}(y|\mathbf{x})$  and  $f(y|\mathbf{x})$ . We assume that  $Y, Y' \in \mathcal{Y} \subseteq \mathbb{R}$  and  $\mathbf{X} \in \mathcal{X} \subseteq \mathbb{R}^d$ , where  $d$  can be large. We also assume that we have access to an i.i.d. sample or “calibration set”  $\mathcal{D} = \{(\mathbf{X}'_1, Y'_1), \dots, (\mathbf{X}'_n, Y'_n)\}$  from the joint distribution  $F_{\mathbf{X}, Y}$  of the target data  $\mathbf{X}$  and  $Y$ . For every fixed  $\mathbf{x} \in \mathcal{X}$ , there exists a unique optimal transport map  $T_{\mathbf{x}} : \mathcal{Y} \rightarrow \mathcal{Y}$  for all strictly convex functions, such that the distribution of  $T_{\mathbf{x}}(Y) := T(Y|\mathbf{x})$  is  $F_{Y|\mathbf{x}}$  (Santambrogio, 2015).

The OT solution performs quantile matching so that  $F(y'_0|\mathbf{x}) = \hat{F}(y_0|\mathbf{x})$ , for every  $y_0 \in \mathcal{Y}$  (as illustrated in the left panel of Figure 2), where the OT map is given by

$$T(y_0|\mathbf{x}) := F^{-1} \left( \hat{F}(y_0|\mathbf{x}) | \mathbf{x} \right). \quad (12)$$



However, it is difficult to perform conditional quantile matching in practice, as the CDF  $F(\cdot|\mathbf{x})$  is unknown and difficult to estimate well across the feature space  $\mathcal{X}$  for high-dimensional covariates  $\mathbf{x}$ . In fact, that was the original motivation for this work.

Instead of conditional quantile matching, the Cal-PIT approach morphs the density  $\hat{f}(y|\mathbf{x})$  into a new density  $\tilde{f}(y|\mathbf{x})$  by mapping probabilities (as illustrated in the right panel of figure 2) through  $\tilde{F}(y_0|\mathbf{x}) := \hat{r}^{\hat{f}}\left(\hat{F}(y_0|\mathbf{x}); \mathbf{x}\right)$ , for every  $y_0 \in \mathcal{Y}$  and  $\mathbf{x} \in \mathcal{X}$ . The value of this approach is that  $\hat{F}(\cdot|\mathbf{x})$  is known, and we can directly compute the conditional P-P map  $\hat{r}^{\hat{f}}(\gamma; \mathbf{x})$  by regressing a scalar quantity against  $\mathbf{x}$  and  $\gamma$  (Algorithm 1). If we have  $\hat{r}^{\hat{f}}$ , we can also easily derive an estimate of the OT solution (Equation 12) for every  $\mathbf{x} \in \mathcal{X}$  by

$$\hat{T}(y_0|\mathbf{x}) := \tilde{F}^{-1}\left(\hat{F}(y_0|\mathbf{x})|\mathbf{x}\right). \quad (13)$$

*Simulation-Based Calibration of Bayesian Posterior Distribution.* In Bayesian inference, the posterior distribution  $F(\theta|\mathbf{x})$  is fundamental for quantifying uncertainty about the parameter  $\theta$  given the data  $\mathbf{x}$ . In many cases, exact computation of the posterior distribution is intractable, and Markov Chain Monte Carlo (MCMC) methods are used to approximate  $F(\theta|\mathbf{x})$  (Robert et al., 1999). Recent advances in machine learning algorithms and simulations have also led to the development of simulation-based inference (SBI; Cranmer et al. 2020) methods that directly *estimate* the posterior distribution  $F(\theta|\mathbf{x})$  from simulated data in settings where the likelihood function is not analytically tractable (Beaumont et al., 2002; Papamakarios & Murray, 2016; Marin et al., 2012; Lueckmann et al., 2017; Sisson et al., 2018; Izbicki et al., 2019; Greenberg et al., 2019).

Cal-PIT can assess the quality of estimated posterior distributions  $\hat{F}(\theta|\mathbf{x})$  from MCMC or Bayesian SBI methods, and if needed, reshape  $\hat{F}(\theta|\mathbf{x})$  to be consistent with the posterior distribution  $F(\theta|\mathbf{x})$  that is associated with the assumed prior and likelihood. For implicit models of  $\hat{F}(\theta|\mathbf{x})$ , such as MCMC, we approximate the PIT values by forward simulating data. Specifically, for a fixed  $\mathbf{x} \in \mathcal{X}$  and  $\theta \in \Theta$ , we draw  $\theta_1, \dots, \theta_L \sim \hat{F}(\cdot|\mathbf{x})$  and approximate  $\text{PIT}(\theta; \mathbf{x})$  using  $L^{-1} \sum_{i=1}^L \mathbb{I}(\theta_i \leq \theta)$ .

Unlike simulation-based calibration (SBC) by Talts et al. (2018), Cal-PIT yields conditionally calibrated posteriors for every instance  $\mathbf{x}$ . More recently, Linhart et al. (2024) provided local diagnostics of CDEs through two-sample testing. However, Cal-PIT offers interpretability regarding potential failure models (such as dispersion and bias) and provides a direct approach for reshaping and morphing the CDEs from a base distribution to the target CDE. The Cal-PIT framework is also different from likelihood-free frequentist inference (LF2I; Dalmasso et al. 2021; Masserano et al. 2022), which constructs and runs diagnostics for frequentist confidence sets based on simulations and a Neyman inversion of hypothesis tests.

*Quantile Regression.* Quantile regression intervals converge to the oracle  $C_\alpha^*(\mathbf{X}) = [F^{-1}(0.5\alpha|\mathbf{X}), F^{-1}(1 - 0.5\alpha|\mathbf{X})]$  (Koenker & Bassett Jr., 1978; Taylor & Bunn, 1999).

Even though the prediction interval  $C_\alpha^*(\mathbf{X})$  satisfies conditional validity,

$$\mathbb{P}(Y \in C_\alpha(\mathbf{X}) | \mathbf{X} = \mathbf{x}) = 1 - \alpha, \quad \forall \mathbf{x} \in \mathcal{X},$$

the standard pinball loss can yield highly miscalibrated UQ models for finite data sets (Chung et al., 2021b; Feldman et al., 2021). New loss functions have been proposed to address this issue (Chung et al., 2021b; Feldman et al., 2021). Our approach also provides calibrated prediction regions but is more general — yielding full CDEs and not only prediction intervals.

*Conformal Inference.* Conformal prediction methods have the appealing property of yielding prediction sets with finite-sample marginal validity,  $\mathbb{P}(Y \in C(\mathbf{X})) \geq 1 - \alpha$ , as long as the data are exchangeable (Vovk et al., 2005; Lei et al., 2018). However, there is no guarantee that conditional validity is satisfied, even approximately. More recent efforts have addressed approximate conditional validity (Romano et al., 2019; Izbicki et al., 2020; Chernozhukov et al., 2021; Izbicki et al., 2022) by designing conformal scores with an approximately homogeneous distribution across  $\mathcal{X}$ . Unfortunately, it is difficult to check whether these methods provide good conditional coverage in practice. Conformal prediction bands are also not conditionally valid, even asymptotically, if the initial model is misspecified. Our method provides estimates of the full CDE. Calibrated CDEs implies calibrated prediction bands but not vice versa.

## Acknowledgments

The authors would like to thank Tria McNeely for helpful discussions and for preparing the tropical cyclone data that were used to fit the TC-inspired model. ABL is grateful to Jing Lei and Larry Wasserman for valuable comments on the P-P map, and to Tudor Manole and Philipp Windischhofer for providing references and a helpful tutorial on Optimal Transport at the workshop “Systematic Effects and Nuisance Parameters in Particle Physic Data Analyses” at Banff, April 2023. BD is a postdoctoral fellow at the University of Toronto in the Eric and Wendy Schmidt AI in Science Postdoctoral Fellowship Program, a program of Schmidt Sciences. This research used resources of the National Energy Research Scientific Computing Center, a DOE Office of Science User Facility supported by the Office of Science of the U.S. Department of Energy under Contract No. DE-AC02-05CH11231 using NERSC award HEP-ERCAP0022859. This work is supported in part by NSF DMS-2053804, NSF PHY-2020295, and the C3.ai Digital Transformation Institute. The efforts of BD and JAN were supported by grant DE-SC0007914 from the U.S. Department of Energy Office of Science, Office of High Energy Physics. BD, BHA, and JAN acknowledge the support of the National Science Foundation under Grant No. AST-2009251. Any opinions, findings, and conclusions, or recommendations expressed in this material are those of the author(s) and do not necessarily reflect the views of the National Science Foundation. RI is grateful for the financial support of CNPq (422705/2021-7 and 305065/2023-8) and FAPESP (2023/07068-1).

## Appendix A. Example 3: Prediction Sets

Cal-PIT’s uniqueness stems from its ability to generate complete CDEs with approximate instance-wise coverage. Additionally, it enables the creation of prediction sets with approximate conditional coverage. Considering the extensive literature on prediction sets, we have included an additional example to demonstrate that prediction sets obtained from Cal-PIT can effectively compete with those derived using methods such as conformal inference or quantile regression. We also include a comparison with normalizing flows, as they have gained popularity for density estimation in the physical sciences.

In photo- $z$  estimation, multiple widely different distances (redshifts) can be consistent with the observed features (colors) of a galaxy. As mentioned previously, this results in conditional distributions that are multi-modal in parts of the feature space. Motivated by the photo- $z$  application, we have modified the two-group example of [Feldman et al. \(2021\)](#) to have bimodal structure due to limited predictor information. Here the target variable  $Y$  depends on three variables:  $X_0, X_1, X_2$ . Variable  $X_0$  indicates group membership but it is not measured; that is,  $X_1$  and  $X_2$  are our only predictors. The missing membership information results in the CDE  $f(y|x_1, x_2)$  being bimodal in the regime  $X_1 > 0$  with one branch corresponding to each class. Supplementary material [S2†](#) details the data-generating process (DGP), and Figure [A1](#) visualizes one random instance of data drawn from  $f(y|x_1, x_2)$  with the “majority” and “minority” groups displayed as blue versus red points.

We design two experiments for benchmarking Cal-PIT prediction sets against results from conformal inference, quantile regression, and normalizing flows:

- Experiment 1 (comparison with conformal inference): For this experiment, we split a sample of total size  $n$  in two halves: the first half is used to train an initial model, and the second half is used for calibration. The empirical coverage of the final prediction sets are computed via 1000 MC simulations from the true DGP at each test point on a grid. Test points with coverage within two standard deviations (SD) of the nominal coverage of  $1 - \alpha = 0.9$  based on 100 random realizations are labeled as having “correct” coverage. We report the proportion of test points in the feature space with “under-,” “correct,” and “over-” coverage.
- Experiment 2 (comparison with quantile regression and normalizing flows): Here we use the entire sample of size  $n$  to compute quantiles or to estimate the conditional density. As above, we use MC simulations on a grid to assess conditional coverage.

The top row of Figure [A2](#) shows results for Experiment 1. We compare 90% prediction sets for  $Y$  using Cal-PIT (INT) and Cal-PIT (HPD) (defined by Equations [7](#) and [D.1](#), respectively) with prediction sets from Reg-split ([Lei et al., 2018](#)), conformalized quantile regression (CQR; [Romano et al. 2019](#)), and distributional conformal prediction (DCP; [Chernozhukov et al. 2021](#)). Reg-split and CQR are trained with XGBoost ([Chen &](#)

† Supplementary Materials: [https://lee-group-cmu.github.io/cal-pit-paper/supplementary\\_material.pdf](https://lee-group-cmu.github.io/cal-pit-paper/supplementary_material.pdf)

Guestrin, 2016). Our Cal-PIT methods use an initial CDE trained using FlexCode with an XGBoost regressor (Izbicki & Lee, 2017; Dalmaso et al., 2020) and monotonic neural networks (Wehenkel & Louppe, 2019) for learning  $\hat{r}^f(\gamma; \mathbf{x})$  with binary cross entropy loss. DCP computes a conformal score based on PIT values derived from the same initial CDE as Cal-PIT. In terms of conditional coverage, all methods improve with increasing sample size, but only Cal-PIT consistently attains the nominal 90% coverage across the feature space for  $n \geq 2000$ . As the data distribution can sometimes be bimodal, the most efficient prediction sets in this feature subspace would not be single intervals (INT), but rather pairs of intervals. We can create such disjoint prediction sets using Highest Predictive Density regions (HPD; see for definition).

The bottom row of Figure A2 shows results for Experiment 2. Cal-PIT (INT) and Cal-PIT (HPD) reshape a uniform distribution on  $\mathbf{x} \in [-5, 5]$ ; hence, there is no need for a separate training set. The Cal-PIT prediction sets are then compared to output from quantile regression (QR; Koenker & Bassett Jr. 1978) trained with XGBoost and a pinball loss, orthogonal quantile regression (OQR; Feldman et al. 2021) which introduces a penalty on the pinball loss to improve conditional coverage, and normalizing flows (NF). We use the PZFlow (Crenshaw et al., 2023) implementation of Normalizing Flows which has been optimized to work well out-of-the-box with tabular data and uses Neural Spline Flows (Dinh et al., 2014, 2016; Durkan et al., 2019) as the backbone.

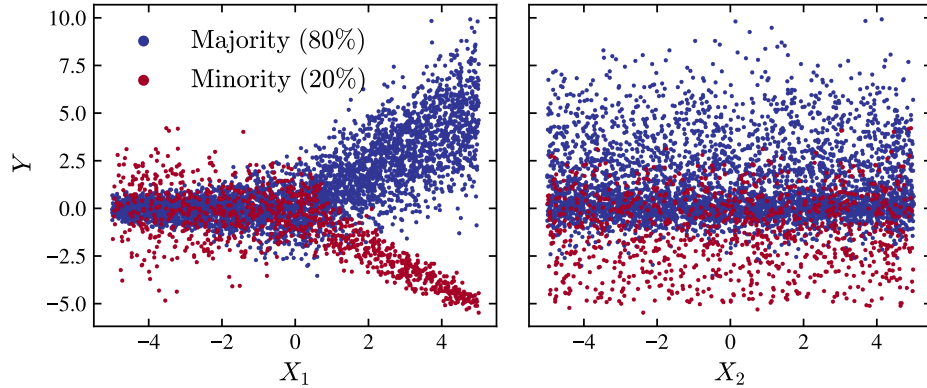


Figure A1: Visualization of one random instance of the data used for Example 1. There are two covariates ( $X_1, X_2$ ), and a target variable  $Y$ . The analytic form of the true data distribution is defined in supplementary material S2. The data set consists of two groups with different spreads.  $Y$  splits into two branches for  $X_1 > 0$ ; that is, the true CDE is bimodal in this region.

Figure A3, top row, shows some examples of calibrated CDEs from Cal-PIT. The estimates reveal that the true conditional density is bimodal for  $X_1 > 0$ ; thus, the most efficient prediction sets in this feature subspace would be HPD regions. Indeed, Cal-PIT (HPD) yields smaller prediction sets than Cal-PIT (INT); see Figure S1 in supplementary material. Because HPD sets can capture the bimodality in the data while intervals cannot, this is a case where Cal-PIT (HPD) has better efficiency. This qualitative insight is only possible because Cal-PIT estimates the entire PDs. Normalizing flows also

provide entire CDEs (see Figure A3, bottom row) but can be difficult to train. Indeed, the normalizing flow CDEs generally deviate significantly from the oracle.

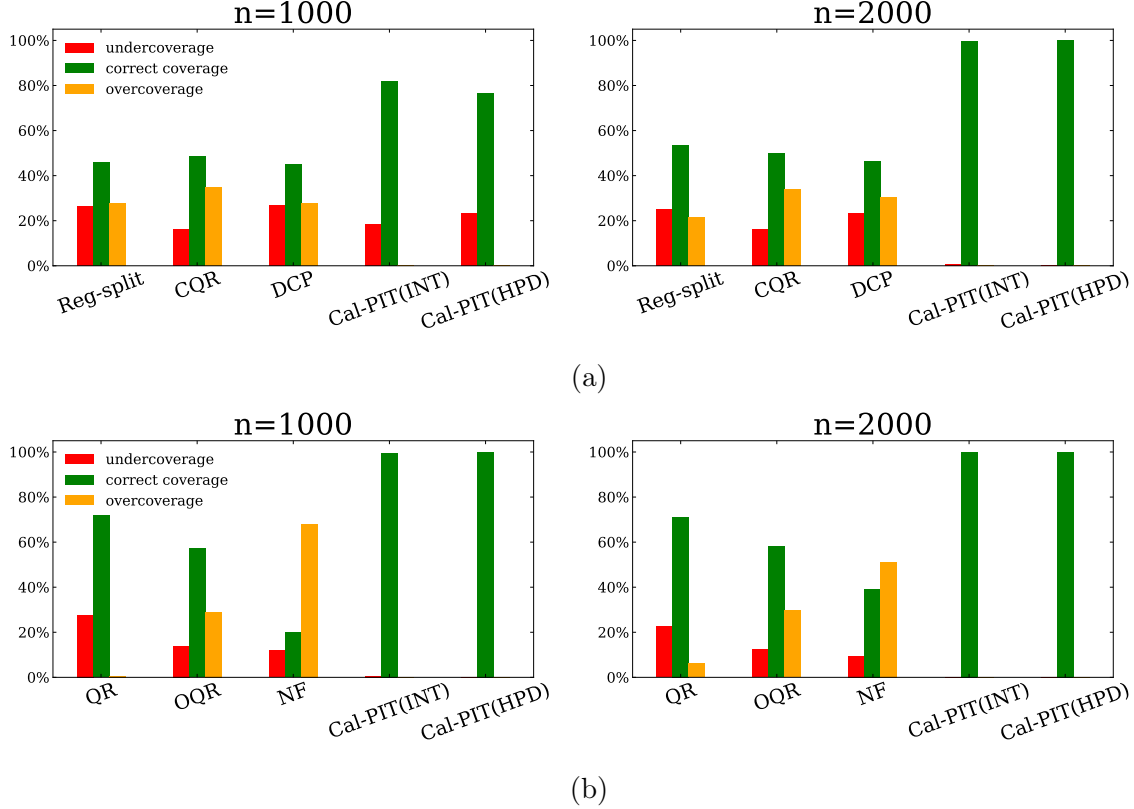
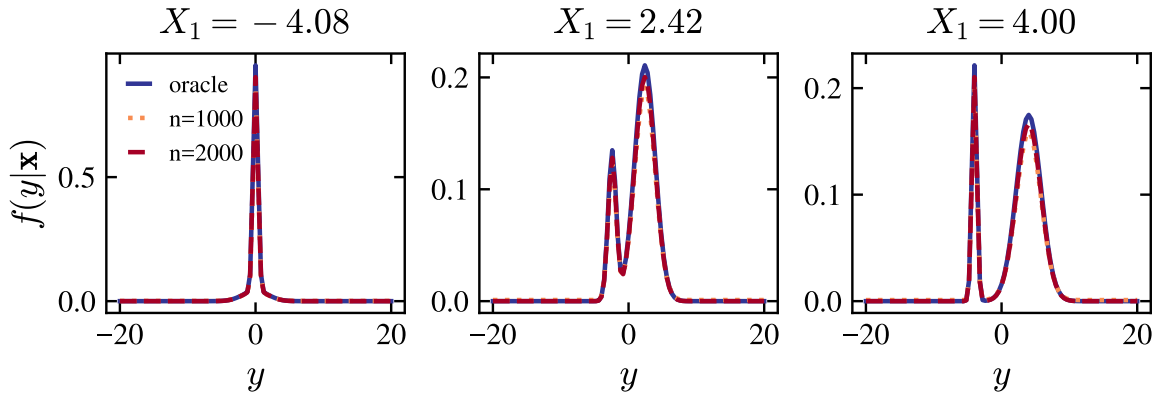
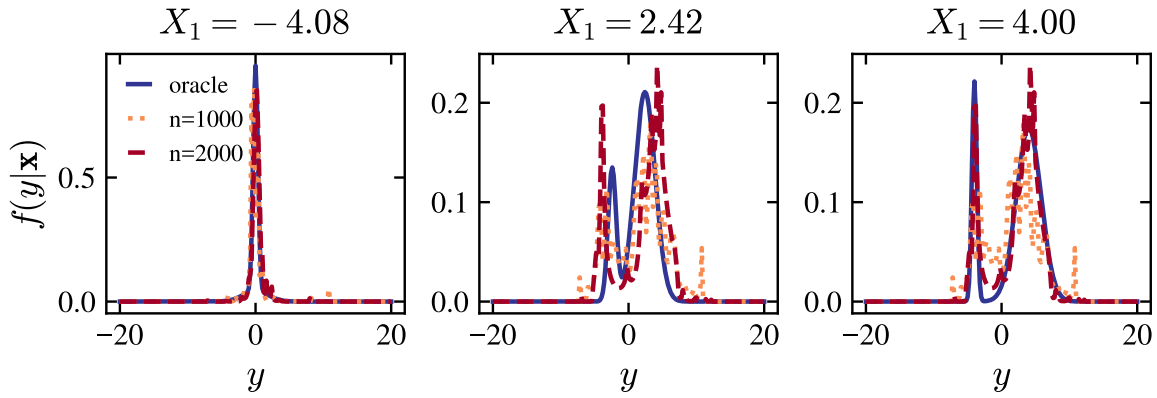


Figure A2: The proportion of test points with correct conditional coverage for (a) “Experiment 1” with state-of-the-art conformal inference methods, using data of total size  $n$  split into a train and a calibration set, and (b) “Experiment 2” with quantile regression and normalizing flow approaches, which use all data for training. See text for details. Only Cal-PIT consistently attains the nominal 90% coverage across the feature space with increasing sample size  $n$ .



(a) CDEs from Cal-PIT



(b) CDEs from Normalizing Flows

Figure A3: CDEs at three different values of  $X_1$  ( $X_2 = 0$ ) for (a) Cal-PIT and (b) Normalizing Flows for Example 3. The results for  $n = 1000$  and  $n = 2000$  are compared to the “oracle” probability density functions. For both sample sizes, the Cal-PIT CDEs are close to the oracle. Normalizing flow CDEs, on the other hand, are harder to train and a standard implementation can deviate significantly from the oracle.



## Appendix B. Local CRPS Scores

The conditional expectation of the CRPS loss given  $\mathbf{X} = \mathbf{x}$  is

$$\mathbb{E} \left[ L_{\text{CRPS}}(\tilde{f}; \mathbf{X}, Y) | \mathbf{x} \right] = \mathbb{E} \left[ \int_{-\infty}^{\infty} \left( \tilde{F}(t|\mathbf{x}) - F(t|\mathbf{x}) + F(t|\mathbf{x}) - \mathbb{I}(Y \leq t) \right)^2 dt | \mathbf{x} \right].$$

By expanding the square and by changing the order of expectation and integration, we have:

$$\begin{aligned} \mathbb{E} \left[ L_{\text{CRPS}}(\tilde{f}; \mathbf{X}, Y) | \mathbf{x} \right] &= \mathbb{E} \left[ \int_{-\infty}^{\infty} \left( \tilde{F}(t|\mathbf{x}) - F(t|\mathbf{x}) \right)^2 dt | \mathbf{x} \right] \\ &\quad + 2 \int_{-\infty}^{\infty} \left( \tilde{F}(t|\mathbf{x}) - F(t|\mathbf{x}) \right) \mathbb{E}[(F(t|\mathbf{x}) - \mathbb{I}(Y \leq t)) dt | \mathbf{x}] \\ &\quad + \int_{-\infty}^{\infty} \mathbb{E}[(F(t|\mathbf{x}) - \mathbb{I}(Y \leq t))^2 | \mathbf{x}] dt. \end{aligned}$$

Note that:

- The first term represents the squared distance between  $\tilde{F}$  and  $F$  and is minimized when  $\tilde{F}(\cdot|\mathbf{x}) = F(\cdot|\mathbf{x})$ .
- The second term equals zero,

$$\mathbb{E}[F(t|\mathbf{x}) - \mathbb{I}(Y \leq t) | \mathbf{x}] = F(t|\mathbf{x}) - \mathbb{E}[\mathbb{I}(Y \leq t) | \mathbf{x}] = F(t|\mathbf{x}) - F(t|\mathbf{x}) = 0.$$

- The third term is a constant that does not depend on  $\tilde{F}$ .

Thus,

$$\begin{aligned} \mathbb{E} \left[ L_{\text{CRPS}}(\tilde{f}; \mathbf{X}, Y) | \mathbf{x} \right] &= \int_{-\infty}^{\infty} \left( \tilde{F}(t|\mathbf{x}) - F(t|\mathbf{x}) \right)^2 dt + K \\ &\approx \int \left( \tilde{F}(Y < t | \mathbf{x}) - \frac{1}{B} \sum_{b=1}^B I(Y_b < t) \right)^2 dt + K \\ &= L_{\text{MC-CRPS}}(\tilde{f}; \mathbf{x}, f) + K, \end{aligned}$$

where  $K$  does not depend on  $\tilde{F}$ .

## Appendix C. Optimal Transport

Here we briefly review Monge's continuous formulation of the OT distance; see [Villani \(2021\)](#) for a more complete and mathematical description of OT.

Consider two distributions  $F_0$  and  $F$  defined over respective domains  $\Omega_0, \Omega \subseteq \mathbb{R}^d$ . Monge's OT problem is to find a function  $T : \Omega_0 \rightarrow \Omega$  that pushes  $F_0$  onto  $F$  and minimizes the distance

$$d(F_0, F) = \inf_T \int \|\mathbf{x} - T(\mathbf{x})\|^p dF_0(\mathbf{x})$$

subject to  $T(\mathbf{X}) \sim F$ , where  $p \geq 1$  and  $\mathbf{X} \sim F_0$ . Such a minimizer  $T^*$  exists if  $F_0$  and  $F$  both have densities. The minimizer  $T^*$  is called the *optimal transport map*. The map

$$T_s(\mathbf{x}) = (1 - s)\mathbf{x} + sT^*(\mathbf{x}), \quad (\text{C.1})$$

for  $s \in [0, 1]$  gives the path of a particle of mass at  $\mathbf{x}$ . The distribution of  $T_s(\mathbf{X})$  is also the geodesic (that is, the shortest path according to the metric  $d$ ) connecting  $F_0$  to  $F$ ; see [Kolouri et al. \(2017\)](#) for a technical definition.

If  $\Omega = \Omega_0 = \mathbb{R}$  and both  $F$  and  $F_0$  are absolutely continuous, with continuous densities which do not vanish, the optimal transport is given by

$$T(x) = F^{-1}(F_0(x)).$$

See [Santambrogio \(2015\)](#) for a detailed survey.

## Appendix D. Cal-PIT (HPD) and Cal-HPD

Here we describe two approaches to deriving prediction sets (instead of prediction intervals) from an estimate of the conditional distribution function  $f(y|\mathbf{x})$ .

### Appendix D.1. Cal-PIT (HPD)

Cal-PIT can also be used to compute Highest Predictive Density regions (HPDs) instead of prediction intervals. The oracle  $(1-\alpha)$ -level HPD set is defined as

$$\text{HPD}_\alpha(\mathbf{x}) = \{y : f(y|\mathbf{x}) \geq t_{\mathbf{x},\alpha}\},$$

where  $t_{\mathbf{x},\alpha}$  is such that  $\int_{y \in \text{HPD}_\alpha(\mathbf{x})} f(y|\mathbf{x}) dy = 1 - \alpha$ . HPDs are the smallest prediction sets that have coverage  $1 - \alpha$ , and thus they may be more precise (smaller set size) than quantile-based intervals, while maintaining the conditional coverage at the nominal level (see supplementary material [S2](#) for an example with a bimodal predictive distribution).

The Cal-PIT estimate of  $\text{HPD}_\alpha(\mathbf{x})$  is given by

$$C_\alpha(\mathbf{x}) = \{y : \tilde{f}(y|\mathbf{x}) \geq \tilde{t}_{\mathbf{x},\alpha}\}, \quad (\text{D.1})$$

where  $\tilde{t}_{\mathbf{x},\alpha}$  is such that  $\int_{y \in C_\alpha(\mathbf{x})} \tilde{f}(y|\mathbf{x}) dy = 1 - \alpha$  and  $\tilde{f}$  is the Cal-PIT calibrated CDE (Algorithm [1](#)).

### Appendix D.2. Cal-HPD

Alternatively, one can directly use HPD values, defined as

$$\hat{H}(y; \mathbf{x}) := \int_{\{y' : \hat{f}(y'|\mathbf{x}) \leq \hat{f}(y|\mathbf{x})\}} \hat{f}(y'|\mathbf{x}) dy',$$

to recalibrate HPD prediction sets (rather than using PIT values). The idea is to estimate the local HPD coverage at each  $\mathbf{x}$ ,  $h^{\hat{f}}(\gamma; \mathbf{x}) := \mathbb{P}(\hat{H}(Y; \mathbf{x}) \leq \gamma|\mathbf{x})$ , by regression,

analogous to estimating the PIT-CDF in Cal-PIT. Let  $\hat{h}^{\hat{f}}(\gamma; \mathbf{x})$  be such an estimate. The recalibrated  $(1 - \alpha)$ -level HPD set at a location  $\mathbf{x}$  is given by the  $(1 - \alpha^*(\mathbf{x}))$ -level HPD set of the original density  $\hat{f}(y|\mathbf{x})$ , where  $\alpha^*(\mathbf{x})$  is such that  $\hat{h}^{\hat{f}}(\alpha^*(\mathbf{x}); \mathbf{x}) = \alpha$ . This framework however does not yield full CDEs. Moreover, although the approach corrects HPD sets, aiming for conditional coverage, the constructed sets will not be optimal if the initial model  $\hat{f}$  is far from the true data generating process  $f$ .

In Example 3 (Appendix A), we only report results for Cal-PIT(INT) and Cal-PIT(HPD); we do not report results for Cal-HPD.

## Appendix E. Local P-Values and Confidence Bands

The *Local Coverage Test* (LCT; Zhao et al. 2021) tests the null hypothesis at fixed  $\mathbf{x}$

$$H_0(\mathbf{x}) : \hat{F}(y|\mathbf{x}) = F(y|\mathbf{x}) \text{ for every } y \in \mathcal{Y}. \quad (\text{E.1})$$

by using the discrepancy score in Equation 8 as a test statistic

$$T(\mathbf{x}) := \frac{1}{|G|} \sum_{\gamma \in G} (\hat{r}^{\hat{f}}(\gamma; \mathbf{x}) - \gamma)^2,$$

where  $G \subset [0, 1]$  is a set of  $\gamma$  values. Large values of  $T(\mathbf{x})$  indicate a large discrepancy between  $\hat{f}$  and  $f$  at  $\mathbf{x}$  in terms of coverage. To find the critical value for rejecting  $H_0(\mathbf{x})$ , LCT uses a Monte Carlo (MC) technique to simulate  $T(\mathbf{x})$  under  $H_0(\mathbf{x})$ . The MC p-value is given by

$$p(\mathbf{x}) := \frac{1}{B} \sum_{b=1}^B \mathbb{I}(T(\mathbf{x}) < T^{(b)}(\mathbf{x})),$$

where  $T^{(b)}(\mathbf{x}) := \frac{1}{|G|} \sum_{\gamma \in G} (\hat{r}^{(b)}(\gamma; \mathbf{x})(\mathbf{x}) - \gamma)^2$ , and  $\hat{r}^{(b)}$  is the regression function of Section 2.3 trained on the  $b$ :th augmented calibration sample  $\mathcal{D}'^{(b)} = \{(\mathbf{X}_i, \gamma_{i,j}, W_{i,j}^{(b)})\}_{i,j}$  for  $i = 1, \dots, n$  and  $j = 1, \dots, K$ , where  $W_{i,j}^{(b)} := \mathbb{I}(U_i^{(b)} \leq \gamma_{i,j})$  and  $U_i^{(b)}$  are independent draws from a uniform distribution over  $(0, 1)$ .

Next, we show that under appropriate conditions, the local p-values are approximately valid. We use the following assumption.

**Assumption 1 (Local regression estimator).** *There exists  $\epsilon > 0$  such that  $\hat{r}$  only uses the sample points in  $\mathcal{D}'$  with  $\mathbf{X}_i \in B(\mathbf{x}; \epsilon)$ , where  $B(\mathbf{x}; \epsilon)$  is a ball of radius  $\epsilon$  centered at  $\mathbf{x}$ .*

Assumption 1 holds for regression estimators that are based on partitions, such as tree-based estimators (e.g., random forests, boosting methods) or smoothing kernel estimators with kernels with bounded support.

**Theorem 2.** *Under the null hypothesis*

$$H_0^\epsilon(\mathbf{x}) : \hat{F}(y|\mathbf{x}') = F(y|\mathbf{x}') \text{ for every } y \in \mathcal{Y} \text{ for all } \mathbf{x}' \in B(\mathbf{x}; \epsilon)$$

and under Assumption 1, for any  $0 < \alpha < 1$

$$\lim_{B \rightarrow \infty} \mathbb{P}(p(\mathbf{x}) \leq \alpha) = \alpha.$$

We can also compute confidence bands for  $\hat{r}^{\hat{f}}(\gamma; \mathbf{x})$  under  $H_0(\mathbf{x})$  by using a similar Monte Carlo technique as above: For a given  $\gamma$ , we can define the lower and upper limits of the  $(1 - \eta)$ -level confidence band for  $\hat{r}^{\hat{f}}(\gamma; \mathbf{x})$  to be the  $\eta/2$  and  $(1 - \eta/2)$  quantiles, respectively, of the set  $\{\hat{r}^{(b)}(\gamma; \mathbf{x})\}_{b=1}^B$ . Such confidence bands are approximately valid as the number of MC repetitions  $B \rightarrow \infty$ .

## Appendix F. Theoretical Properties of Cal-PIT

We here describe the assumptions needed for Theorem 1, and provide convergence rates. We also prove that Cal-PIT intervals achieve asymptotic conditional validity even if the initial CDE  $\hat{f}$  is not consistent. The following results are conditional on  $\hat{f}$ ; all uncertainty refers to the calibration sample. We assume in Theorem 1 that the true distribution of  $Y|\mathbf{x}$  and its initial estimate are continuous, and that  $\hat{F}$  places its mass on a region that is at least as large as that of  $F$ :

**Assumption 2** (Continuity of the cumulative distribution functions). *For every  $\mathbf{x} \in \mathcal{X}$ ,  $\hat{F}(\cdot|\mathbf{x})$  and  $F(\cdot|\mathbf{x})$  are continuous functions.*

**Assumption 3** ( $\hat{F}$  dominates  $F$ ). *For every  $\mathbf{x} \in \mathcal{X}$ ,  $\hat{F}(\cdot|\mathbf{x})$  dominates  $F(\cdot|\mathbf{x})$ .*

We also assume that  $F(\cdot|\mathbf{x})$  cannot place too much mass in regions where the initial estimate  $\hat{F}(\cdot|\mathbf{x})$  places little mass:

**Assumption 4** (Bounded density). *There exists  $K > 0$  such that, for every  $\mathbf{x} \in \mathcal{X}$ , the Radon-Nikodym derivative of  $F(\cdot|\mathbf{x})$  with respect to  $\hat{F}(\cdot|\mathbf{x})$  is bounded above by  $K$ .*

To provide rates of convergence for the recalibrated CDE, we will in addition assume that the regression method converges at a rate  $O(n^{-\kappa})$ :

**Assumption 5** (Convergence rate of the regression method). *The regression method used to estimate  $r^{\hat{f}}$  is such that its convergence rate is given by*

$$\mathbb{E} \left[ \int \int \left( \hat{r}^{\hat{f}}(\gamma; \mathbf{x}) - r^{\hat{f}}(\gamma; \mathbf{x}) \right)^2 d\gamma dP(\mathbf{x}) \right] = O \left( \frac{1}{n^\kappa} \right)$$

for some  $\kappa > 0$ .

Many methods satisfy Assumption 5 for some value  $\kappa$ , which is typically related to the dimension of  $\mathcal{X}$  and the smoothness of the true regression  $r$  (see for instance Györfi et al. 2002).

Under these assumptions, we can derive the rate of convergence for  $\tilde{F}$ :

**Corollary 1** (Convergence rate of recalibrated CDE). *Under Assumptions 2, 3, 4 and 5,*

$$\mathbb{E} \left[ \int \int \left( \tilde{F}(y|\mathbf{x}) - F(y|\mathbf{x}) \right)^2 dP(y, \mathbf{x}) \right] = O \left( \frac{1}{n^\kappa} \right). \quad (\text{F.1})$$

Next, we show that with an uniformly consistent regression estimator  $\hat{r}^{\hat{f}}(\gamma; \mathbf{x})$  (see Bierens 1983; Hardle et al. 1984; Liero 1989; Girard et al. 2014 for some examples), Cal-PIT intervals achieve asymptotic conditional validity, even if the initial CDE  $\hat{f}(y|\mathbf{x})$  is not consistent.

**Assumption 6** (Uniform consistency of the regression estimator). *The regression estimator is such that*

$$\sup_{\mathbf{x} \in \mathcal{X}, \gamma \in [0,1]} |\hat{r}^{\hat{f}}(\gamma; \mathbf{x}) - r^{\hat{f}}(\gamma; \mathbf{x})| \xrightarrow[n \rightarrow \infty]{a.s.} 0,$$

where the convergence is with respect to the calibration set  $\mathcal{D}$  only;  $\hat{f}$  is fixed.

**Theorem 3** (Consistency and conditional coverage of Cal-PIT intervals). *Let  $C_\alpha^*(\mathbf{x}) = [F^{-1}(0.5\alpha|\mathbf{x}); F^{-1}(1 - 0.5\alpha|\mathbf{x})]$  be the oracle prediction band, and let  $C_\alpha^n(\mathbf{x})$  denote the Cal-PIT interval. Under Assumptions 2, 3 and 6,*

$$\lambda(C_\alpha^n(\mathbf{X}) \Delta C_\alpha^*(\mathbf{X})) \xrightarrow[n \rightarrow \infty]{a.s.} 0, \quad (\text{F.2})$$

where  $\lambda$  is the Lebesgue measure in  $\mathbb{R}$  and  $\Delta$  is the symmetric difference between two sets. It follows that  $C_\alpha^n(\mathbf{X})$  has asymptotic conditional coverage of  $1 - \alpha$  (Lei et al., 2018).

See Appendix G.1 for theoretical results for Cal-PIT (HPD).

## Appendix G. Proofs

**Lemma 1.** *Let  $G$  and  $H$  be two cumulative distribution functions such that  $G$  dominates  $H$ , and let  $\mu_G$  and  $\mu_H$  be their associated measures over  $\mathbb{R}$ . Then, for every fixed  $y \in \mathbb{R}$ ,*

$$\mu_H(\{y' \in \mathbb{R} : y' \leq y\}) = \mu_H(\{y' \in \mathbb{R} : G(y') \leq G(y)\}).$$

*Proof.* Fix  $y \in \mathbb{R}$  and let  $A = \{y' \in \mathbb{R} : y' \leq y\}$  and  $B = \{y' \in \mathbb{R} : G(y') \leq G(y)\}$ . Because  $A \subseteq B$ ,

$$\mu_H(A) \leq \mu_H(B). \quad (\text{G.1})$$

We note that  $\mu_G(B \cap A^c) = 0$ . From this and the assumption that  $G$  dominates  $H$ , we conclude that  $\mu_H(B \cap A^c) = 0$ . It follows that

$$\begin{aligned} \mu_H(B) &= \mu_H(B \cap A) + \mu_H(B \cap A^c) \leq \mu_H(A) + 0 \\ &= \mu_H(A). \end{aligned} \quad (\text{G.2})$$

From Equations G.1 and G.2, we conclude that  $\mu_H(A) = \mu_H(B)$ .

□

**Lemma 2.** Fix  $y \in \mathbb{R}$  and let  $\gamma := \widehat{F}(y|\mathbf{x})$ . Then, under Assumptions 2 and 3,  $\widetilde{F}(y|\mathbf{x}) = \widehat{r}^{\widehat{F}}(\gamma; \mathbf{x})$  and  $F(y|\mathbf{x}) = r^{\widehat{F}}(\gamma; \mathbf{x})$ .

*Proof.* We note that  $\gamma = \widehat{F}(y|\mathbf{x})$  implies that  $y = \widehat{F}^{-1}(\gamma|\mathbf{x})$ . It follows then by construction,

$$\widetilde{F}(y|\mathbf{x}) = \widetilde{F}\left(\widehat{F}^{-1}(\gamma|\mathbf{x})|\mathbf{x}\right) = \widehat{r}^{\widehat{F}}(\gamma; \mathbf{x}).$$

Moreover,

$$\begin{aligned} F(y|\mathbf{x}) &= \mathbb{P}(Y \leq y|\mathbf{x}) \\ &= \mathbb{P}\left(\widehat{F}(Y|\mathbf{x}) \leq \widehat{F}(y|\mathbf{x})|\mathbf{x}\right) \\ &\quad (\text{Assumption 3 and Lemma 1}) \\ &= \mathbb{P}\left(\text{PIT}(Y; \mathbf{x}) \leq \widehat{F}(y|\mathbf{x})|\mathbf{x}\right) \\ &= \mathbb{P}(\text{PIT}(Y; \mathbf{x}) \leq \gamma|\mathbf{x}) \\ &= r^{\widehat{F}}(\gamma; \mathbf{x}), \end{aligned}$$

which concludes the proof.  $\square$

*Proof of Theorem 1.* Consider the change of variables  $\gamma = \widehat{F}(y|\mathbf{x})$ , so that  $d\gamma = \widehat{f}(y|\mathbf{x})dy$ . Lemma 2 implies that  $\widetilde{F}(y|\mathbf{x}) = \widehat{r}^{\widehat{F}}(\gamma; \mathbf{x})$  and  $F(y|\mathbf{x}) = r^{\widehat{F}}(\gamma; \mathbf{x})$ . It follows from that and Assumption 4 that

$$\begin{aligned} &\int \int \left(\widetilde{F}(y|\mathbf{x}) - F(y|\mathbf{x})\right)^2 dP(y, \mathbf{x}) \\ &\leq K \int \int \left(\widetilde{F}(y|\mathbf{x}) - F(y|\mathbf{x})\right)^2 \widehat{f}(y|\mathbf{x}) dy P(\mathbf{x}) \\ &= K \int \int \left(\widehat{r}^{\widehat{F}}(\gamma; \mathbf{x}) - r^{\widehat{F}}(\gamma; \mathbf{x})\right)^2 d\gamma dP(\mathbf{x}), \end{aligned}$$

which concludes the proof.  $\square$

*Proof of Corollary 1.* Follows directly from Assumption 5 and Theorem 1.  $\square$

*Proof of Theorem 3.* From Lemma 2,

$$\begin{aligned} &\sup_{\mathbf{x} \in \mathcal{X}, y \in \mathbb{R}} |\widetilde{F}(y|\mathbf{x}) - F(y|\mathbf{x})| \\ &= \sup_{\mathbf{x} \in \mathcal{X}, \gamma \in [0,1]} |\widehat{r}^{\widehat{F}}(\gamma; \mathbf{x}) - r^{\widehat{F}}(\gamma; \mathbf{x})| \xrightarrow[n \rightarrow \infty]{\text{a.s.}} 0, \end{aligned}$$

where the last step follows from Assumption 6. It then follows from Assumption 2 that

$$\sup_{\mathbf{x} \in \mathcal{X}, \gamma \in [0,1]} |\widetilde{F}^{-1}(\gamma|\mathbf{x}) - F^{-1}(\gamma|\mathbf{x})| \xrightarrow[n \rightarrow \infty]{\text{a.s.}} 0,$$

and, in particular,

$$\sup_{\mathbf{x} \in \mathcal{X}, \alpha \in \{.5\alpha, 1 - .5\alpha\}} |\widetilde{F}^{-1}(\alpha|\mathbf{x}) - F^{-1}(\alpha|\mathbf{x})| \xrightarrow[n \rightarrow \infty]{\text{a.s.}} 0,$$

from which the conclusion of the theorem follows.  $\square$



## Appendix G.1. Theory for Cal-PIT HPD sets

For every  $\mathbf{x} \in \mathcal{X}$ , let  $C_\alpha(\mathbf{x}) = \{y : \tilde{f}(y|\mathbf{x}) \geq \tilde{t}_{\mathbf{x},\alpha}\}$ , where  $\tilde{t}_{\mathbf{x},\alpha}$  is such that  $\int_{y \in C_\alpha(\mathbf{x})} \tilde{f}(y|\mathbf{x}) dy = 1 - \alpha$  be the Cal-PIT HPD-set. Similarly, let  $\text{HPD}_\alpha(\mathbf{x}) = \{y : f(y|\mathbf{x}) \geq t_{\mathbf{x},\alpha}\}$ , where  $t_{\mathbf{x},\alpha}$  is such that  $\int_{y \in \text{HPD}_\alpha(\mathbf{x})} f(y|\mathbf{x}) dy = 1 - \alpha$  be the true HPD-set. The next theorem shows that if the probabilistic classifier is well estimated, then Cal-PIT HPD sets are exactly equivalent to oracle HPD sets.

**Theorem 4** (Fisher consistency Cal-PIT HPD-sets). *Fix  $\mathbf{x} \in \mathcal{X}$ . If  $\hat{r}(\gamma; \mathbf{x}) = r(\gamma; \mathbf{x})$  for every  $\gamma \in [0, 1]$ ,  $C_\alpha(\mathbf{x}) = \text{HPD}_\alpha(\mathbf{x})$  and  $\mathbb{P}(Y \in C_\alpha(\mathbf{X})|\mathbf{x}) = 1 - \alpha$ .*

*Proof of Theorem 4.* Fix  $y \in \mathbb{R}$  and let  $\gamma = \hat{F}(y|\mathbf{x})$ , so that  $y = \hat{F}^{-1}(\gamma|\mathbf{x})$ . It follows that

$$\begin{aligned} \tilde{F}(y|\mathbf{x}) &= \tilde{F}\left(\hat{F}^{-1}(\gamma|\mathbf{x})|\mathbf{x}\right) = \hat{r}(\gamma; \mathbf{x}) = r(\gamma; \mathbf{x}) \\ &= \mathbb{P}\left(\hat{F}(Y|\mathbf{x}) \leq \hat{F}(y|\mathbf{x})|\mathbf{x}, \gamma\right) = \mathbb{P}(Y \leq y|\mathbf{x}, \gamma) \\ &= F(y|\mathbf{x}), \end{aligned}$$

and therefore  $\tilde{f}(y|\mathbf{x}) = f(y|\mathbf{x})$  for almost every  $y \in \mathbb{R}$ . It follows that  $C_\alpha(\mathbf{x}) = \text{HPD}_\alpha(\mathbf{x})$ . The claim about conditional coverage follows from the definition of the HPD.  $\square$

*Proof of Theorem 2.* Notice that, under  $H_0^\epsilon(\mathbf{x})$ , for every  $\mathbf{x}' \in B(\mathbf{x}; \epsilon)$ ,

$$\text{PIT}(Y_i; \mathbf{X}_i)|\mathbf{X}_i = \mathbf{x}' \sim \text{Unif}(0, 1),$$

and therefore

$$(\mathbf{X}_i, \gamma_{i,j}, W_{i,j}^{(b)})|\mathbf{X}_i = \mathbf{x}', \gamma_{i,j} \stackrel{\text{i.i.d.}}{\sim} (\mathbf{X}_i, \gamma_{i,j}, W_{i,j})|\mathbf{X}_i = \mathbf{x}', \gamma_{i,j}.$$

It follows that

$$\mathcal{D}'_{\mathbf{x}}|\mathcal{C} \stackrel{\text{i.i.d.}}{\sim} \mathcal{D}_{\mathbf{x}}^{(b)}|\mathcal{C},$$

where

$$\begin{aligned} \mathcal{C} &= \{(\mathbf{X}_i, \gamma_{i,j})\}_{i,j}, \\ \mathcal{D}'_{\mathbf{x}} &= \{(\mathbf{X}_i, \gamma_{i,j}, W_{i,j}) \in \mathcal{D}' : \mathbf{X}_i \in B(\mathbf{x}; \epsilon)\} \end{aligned}$$

and

$$\mathcal{D}_{\mathbf{x}}^{(b)} := \left\{(\mathbf{X}_i, \gamma_{i,j}, W_{i,j}^{(b)}) \in \mathcal{D}^{(b)} : \mathbf{X}_i \in B(\mathbf{x}; \epsilon)\right\}.$$

Now by Assumption 1,  $T(\mathbf{x})$  (similarly,  $T^{(b)}(\mathbf{x})$ ) is a function of  $\mathcal{D}'_{\mathbf{x}}$  (similarly,  $\mathcal{D}_{\mathbf{x}}^{(b)}$ ). It follows that

$$T(\mathbf{x})|\mathcal{C} \stackrel{\text{i.i.d.}}{\sim} T^{(b)}(\mathbf{x})|\mathcal{C}.$$

Thus, by the law of large numbers, for every fixed augmented dataset  $\mathcal{D}' = d_{\text{obs}}$ ,

$$\begin{aligned} p(\mathbf{x})|\mathcal{C}, \mathcal{D}' = d_{\text{obs}} &\xrightarrow[B \rightarrow \infty]{\text{a.s.}} \mathbb{P}(T_{\mathcal{D}'=d_{\text{obs}}}(\mathbf{x}) < T_{\mathcal{D}'}(\mathbf{x})|\mathcal{C}) \\ &= 1 - F_{T_{\mathcal{D}'}(\mathbf{x})|\mathcal{C}}(T_{\mathcal{D}'=d_{\text{obs}}}(\mathbf{x})), \end{aligned}$$

where  $T_{\mathcal{D}'=d_{\text{obs}}}$  is the test statistic computed at  $\mathcal{D}' = d_{\text{obs}}$ , and hence

$$p(\mathbf{x})|\mathcal{C} \xrightarrow[B \rightarrow \infty]{\mathcal{L}} 1 - F_{T_{\mathcal{D}'(\mathbf{x})}|\mathcal{C}}(T_{\mathcal{D}'}(\mathbf{x})),$$

The conclusion follows from the fact that  $F_{T_{\mathcal{D}'(\mathbf{x})}|\mathcal{C}}(T_{\mathcal{D}'}(\mathbf{x}))$  is a uniform random variable, and therefore so is  $1 - F_{T_{\mathcal{D}'(\mathbf{x})}|\mathcal{C}}(T_{\mathcal{D}'}(\mathbf{x}))$ .  $\square$

## Appendix G.2. Further Details on Experiments

We refer the reader to the online supplementary materials for details on the training of the regression model to learn the PIT-CDF function in our experiments, further remarks on Example 3 (prediction sets) results, and a description of the synthetic data generation and the training of the initial ConvMDN model in Example 2.

## References

- Akeson, R., Armus, L., Bachelet, E., et al. 2019, The Wide Field Infrared Survey Telescope: 100 Hubbles for the 2020s, arXiv e-prints, arXiv:1902.05569, doi: [10.48550/arXiv.1902.05569](https://doi.org/10.48550/arXiv.1902.05569)
- Alkema, L., Raftery, A. E., & Clark, S. J. 2007, Probabilistic projections of HIV prevalence using Bayesian melding, *The annals of applied statistics*, 1, 229
- Almosallam, I. A., Jarvis, M. J., & Roberts, S. J. 2016, GPZ: non-stationary sparse Gaussian processes for heteroscedastic uncertainty estimation in photometric redshifts, *MNRAS*, 462, 726, doi: [10.1093/mnras/stw1618](https://doi.org/10.1093/mnras/stw1618)
- Ambrogioni, L., Güçlü, U., van Gerven, M. A. J., & Maris, E. 2017, The Kernel Mixture Network: A Nonparametric Method for Conditional Density Estimation of Continuous Random Variables, arXiv e-prints, arXiv:1705.07111. <https://arxiv.org/abs/1705.07111>
- Amerise, I. L. 2018, Quantile Regression Estimation Using Non-Crossing Constraints, *Journal of Mathematics and Statistics*, 14, 107, doi: [10.3844/jmssp.2018.107.118](https://doi.org/10.3844/jmssp.2018.107.118)
- Andrews, D. W. K. 1997, A conditional Kolmogorov test, *Econometrica*, 65, 1097
- Arnouts, S., Cristiani, S., Moscardini, L., et al. 1999, Measuring and modelling the redshift evolution of clustering: the Hubble Deep Field North, *MNRAS*, 310, 540, doi: [10.1046/j.1365-8711.1999.02978.x](https://doi.org/10.1046/j.1365-8711.1999.02978.x)
- Beaumont, M. A., Zhang, W., & Balding, D. J. 2002, Approximate Bayesian computation in population genetics, *Genetics*, 162, 2025
- Beck, R., Dobos, L., Budavári, T., Szalay, A. S., & Csabai, I. 2016, Photometric redshifts for the SDSS Data Release 12, *MNRAS*, 460, 1371, doi: [10.1093/mnras/stw1009](https://doi.org/10.1093/mnras/stw1009)
- Benítez, N. 2000, Bayesian Photometric Redshift Estimation, *ApJ*, 536, 571, doi: [10.1086/308947](https://doi.org/10.1086/308947)

- Bierens, H. J. 1983, Uniform consistency of kernel estimators of a regression function under generalized conditions, *Journal of the American Statistical Association*, 78, 699
- Bishop, C. M. 1994. <https://publications.aston.ac.uk/id/eprint/373/>
- Bordoloi, R., Lilly, S. J., & Amara, A. 2010, Photo-z performance for precision cosmology, *Monthly Notices of the Royal Astronomical Society*, 406, 881. <https://doi.org/10.1111/j.1365-2966.2010.16765.x>
- Brammer, G. B., van Dokkum, P. G., & Coppi, P. 2008, EAZY: A Fast, Public Photometric Redshift Code, *ApJ*, 686, 1503, doi: [10.1086/591786](https://doi.org/10.1086/591786)
- Carrasco Kind, M., & Brunner, R. J. 2013, TPZ: photometric redshift PDFs and ancillary information by using prediction trees and random forests, *MNRAS*, 432, 1483, doi: [10.1093/mnras/stt574](https://doi.org/10.1093/mnras/stt574)
- Cavuoti, S., Amaro, V., Brescia, M., et al. 2017, METAPHOR: a machine-learning-based method for the probability density estimation of photometric redshifts, *MNRAS*, 465, 1959, doi: [10.1093/mnras/stw2930](https://doi.org/10.1093/mnras/stw2930)
- Chen, T., & Guestrin, C. 2016, in *Proceedings of the 22nd ACM SIGKDD International Conference on Knowledge Discovery and Data Mining, KDD '16* (New York, NY, USA: ACM), 785–794, doi: [10.1145/2939672.2939785](https://doi.org/10.1145/2939672.2939785)
- Chen, T. Y., Dey, B., Ghosh, A., et al. 2022, Interpretable Uncertainty Quantification in AI for HEP, *Proceedings of the US Community Study on the Future of Particle Physics (Snowmass 2021)*, arXiv:2208.03284. <https://arxiv.org/abs/2208.03284>
- Chernozhukov, V., Wüthrich, K., & Zhu, Y. 2021, Distributional conformal prediction, *Proceedings of the National Academy of Sciences*, 118
- Chung, Y., Neiswanger, W., Char, I., & Schneider, J. 2021a, in *Advances in Neural Information Processing Systems 34: Annual Conference on Neural Information Processing Systems 2021, NeurIPS 2021, December 6-14, 2021, virtual*, ed. M. Ranzato, A. Beygelzimer, Y. N. Dauphin, P. Liang, & J. W. Vaughan, 10971–10984. <https://proceedings.neurips.cc/paper/2021/hash/5b168fdb5ee5ea262cc2d4c0b457697-Abstract.html>
- Chung, Y., Neiswanger, W., Char, I., & Schneider, J. 2021b, in *Advances in Neural Information Processing Systems*, Vol. 35 (Curran Associates, Inc.)
- Conroy, C. 2013, Modeling the Panchromatic Spectral Energy Distributions of Galaxies, *ARA&A*, 51, 393, doi: [10.1146/annurev-astro-082812-141017](https://doi.org/10.1146/annurev-astro-082812-141017)
- Cook, S. R., Gelman, A., & Rubin, D. B. 2006, Validation of software for Bayesian models using posterior quantiles, *Journal of Computational and Graphical Statistics*, 15, 675
- Cranmer, K., Brehmer, J., & Louppe, G. 2020, The frontier of simulation-based inference, *Proceedings of the National Academy of Sciences*, 117, 30055
- Crenshaw, J. F., Yan, Z., & vladislav doster. 2023, jfcrenshaw/pzflow: v3.1.1, v3.1.1, Zenodo, doi: [10.5281/zenodo.7843901](https://doi.org/10.5281/zenodo.7843901)

- Dalmaso, N., Masserano, L., Zhao, D., Izbicki, R., & Lee, A. B. 2021, Likelihood-Free Frequentist Inference: Confidence Sets with Correct Conditional Coverage, arXiv preprint arXiv:2107.03920
- Dalmaso, N., Pospisil, T., Lee, A., et al. 2020, Conditional density estimation tools in python and R with applications to photometric redshifts and likelihood-free cosmological inference, *Astronomy and Computing*, 30, 100362, doi: [10.1016/j.ascom.2019.100362](https://doi.org/10.1016/j.ascom.2019.100362)
- Dalmaso, N., Pospisil, T., Lee, A. B., et al. 2020, Conditional density estimation tools in python and R with applications to photometric redshifts and likelihood-free cosmological inference, *Astronomy and Computing*, 30, 100362, doi: [10.1016/j.ascom.2019.100362](https://doi.org/10.1016/j.ascom.2019.100362)
- DeMaria, M., Sampson, C. R., Knaff, J. A., & Musgrave, K. D. 2014, Is Tropical Cyclone Intensity Guidance Improving?, *Bulletin of the American Meteorological Society*, 95, 387, doi: [10.1175/BAMS-D-12-00240.1](https://doi.org/10.1175/BAMS-D-12-00240.1)
- DeRose, J., Wechsler, R. H., Becker, M. R., et al. 2019, The buzzard flock: Dark energy survey synthetic sky catalogs, arXiv preprint arXiv:1901.02401
- DESI Collaboration, Abareshi, B., Aguilar, J., et al. 2022, Overview of the Instrumentation for the Dark Energy Spectroscopic Instrument, *AJ*, 164, 207, doi: [10.3847/1538-3881/ac882b](https://doi.org/10.3847/1538-3881/ac882b)
- Dey, A., Schlegel, D. J., Lang, D., et al. 2019, Overview of the DESI Legacy Imaging Surveys, *AJ*, 157, 168, doi: [10.3847/1538-3881/ab089d](https://doi.org/10.3847/1538-3881/ab089d)
- Dey, B., Andrews, B. H., Newman, J. A., et al. 2022, Photometric redshifts from SDSS images with an interpretable deep capsule network, *MNRAS*, 515, 5285, doi: [10.1093/mnras/stac2105](https://doi.org/10.1093/mnras/stac2105)
- Dey, B., Newman, J. A., Andrews, B. H., et al. 2021, Re-calibrating Photometric Redshift Probability Distributions Using Feature-space Regression, arXiv e-prints, arXiv:2110.15209, doi: [10.48550/arXiv.2110.15209](https://doi.org/10.48550/arXiv.2110.15209)
- Dhariwal, P., & Nichol, A. Q. 2021, in *Advances in Neural Information Processing Systems 34: Annual Conference on Neural Information Processing Systems 2021, NeurIPS 2021, December 6-14, 2021, virtual*, ed. M. Ranzato, A. Beygelzimer, Y. N. Dauphin, P. Liang, & J. W. Vaughan, 8780–8794. <https://proceedings.neurips.cc/paper/2021/hash/49ad23d1ec9fa4bd8d77d02681df5cfa-Abstract.html>
- Dinh, L., Krueger, D., & Bengio, Y. 2014, NICE: Non-linear Independent Components Estimation, arXiv e-prints, arXiv:1410.8516, doi: [10.48550/arXiv.1410.8516](https://doi.org/10.48550/arXiv.1410.8516)
- Dinh, L., Sohl-Dickstein, J., & Bengio, S. 2016, Density estimation using Real NVP, arXiv e-prints, arXiv:1605.08803, doi: [10.48550/arXiv.1605.08803](https://doi.org/10.48550/arXiv.1605.08803)
- Durkan, C., Bekasov, A., Murray, I., & Papamakarios, G. 2019, Neural Spline Flows, arXiv e-prints, arXiv:1906.04032, doi: [10.48550/arXiv.1906.04032](https://doi.org/10.48550/arXiv.1906.04032)
- Dutordoir, V., Salimbeni, H., Hensman, J., & Deisenroth, M. P. 2018, in *Advances in Neural Information Processing Systems 31: Annual Conference on Neural Information*

- Processing Systems 2018, NeurIPS 2018, December 3-8, 2018, Montréal, Canada, ed. S. Bengio, H. M. Wallach, H. Larochelle, K. Grauman, N. Cesa-Bianchi, & R. Garnett, 2391–2401. <https://proceedings.neurips.cc/paper/2018/hash/6a61d423d02a1c56250dc23ae7ff12f3-Abstract.html>
- D’Isanto, A., & Polsterer, K. L. 2018, Photometric redshift estimation via deep learning. Generalized and pre-classification-less, image based, fully probabilistic redshifts, *Astronomy & Astrophysics*, 609, A111
- Euclid Collaboration, Ilbert, O., de la Torre, S., et al. 2021, Euclid preparation. XI. Mean redshift determination from galaxy redshift probabilities for cosmic shear tomography, *A&A*, 647, A117, doi: [10.1051/0004-6361/202040237](https://doi.org/10.1051/0004-6361/202040237)
- Fasiolo, M., Wood, S. N., Zaffran, M., Nedellec, R., & Goude, Y. 2021, Fast Calibrated Additive Quantile Regression, *Journal of the American Statistical Association*, 116, 1402, doi: [10.1080/01621459.2020.1725521](https://doi.org/10.1080/01621459.2020.1725521)
- Feldman, S., Bates, S., & Romano, Y. 2021, Improving Conditional Coverage via Orthogonal Quantile Regression, *arXiv*, 1. <https://arxiv.org/abs/2106.00394>
- Freeman, P., Izbicki, R., & Lee, A. B. 2017, A unified framework for constructing, tuning and assessing photometric redshift density estimates in a selection bias setting, *Monthly Notices of the Royal Astronomical Society*, 468, 4556, doi: [10.1093/mnras/stx764](https://doi.org/10.1093/mnras/stx764)
- Gaia Collaboration, Prusti, T., de Bruijne, J. H. J., et al. 2016, The Gaia mission, *A&A*, 595, A1, doi: [10.1051/0004-6361/201629272](https://doi.org/10.1051/0004-6361/201629272)
- Gal, Y., & Ghahramani, Z. 2016, in *International Conference on Machine Learning, Proceedings of Machine Learning Research (PMLR)*, 1050–1059
- Gan, F. F., & Koehler, K. J. 1990, Goodness-of-Fit Tests Based on P-P Probability Plots, *Technometrics*, 32, 289, doi: [10.1080/00401706.1990.10484682](https://doi.org/10.1080/00401706.1990.10484682)
- Girard, S., Guillou, A., & Stupfler, G. 2014, Uniform strong consistency of a frontier estimator using kernel regression on high order moments, *ESAIM: Probability and Statistics*, 18, 642
- Gneiting, T. 2008, Probabilistic forecasting, *Journal of the Royal Statistical Society. Series A (Statistics in Society)*, 319
- Gneiting, T., & Katzfuss, M. 2014, Probabilistic Forecasting, *Annual Review of Statistics and Its Application*, 1, 125, doi: [10.1146/annurev-statistics-062713-085831](https://doi.org/10.1146/annurev-statistics-062713-085831)
- Goan, E., & Fookes, C. 2020, Bayesian Neural Networks: An Introduction and Survey, *CoRR*, abs/2006.12024
- Good, I. J. 1952, Rational Decisions, *Journal of the Royal Statistical Society. Series B (Methodological)*, 14, 107. <http://www.jstor.org/stable/2984087>
- Graff, P., Feroz, F., Hobson, M. P., & Lasenby, A. 2014, SKYNET: an efficient and robust neural network training tool for machine learning in astronomy, *MNRAS*, 441, 1741, doi: [10.1093/mnras/stu642](https://doi.org/10.1093/mnras/stu642)

- Graham, M. L., Connolly, A. J., Ivezić, Ž., et al. 2018, Photometric Redshifts with the LSST: Evaluating Survey Observing Strategies, *AJ*, 155, 1, doi: [10.3847/1538-3881/aa99d4](https://doi.org/10.3847/1538-3881/aa99d4)
- Greenberg, D., Nonnenmacher, M., & Macke, J. 2019, in *International Conference on Machine Learning*, PMLR, 2404–2414
- Griffin, S. M., Wimmers, A., & Velden, C. S. 2022, Predicting Rapid Intensification in North Atlantic and Eastern North Pacific Tropical Cyclones using a Convolutional Neural Network, *Weather and Forecasting*
- Guo, C., Pleiss, G., Sun, Y., & Weinberger, K. Q. 2017, in *Proceedings of Machine Learning Research*, Vol. 70, *Proceedings of the 34th International Conference on Machine Learning*, ed. D. Precup & Y. W. Teh (PMLR), 1321–1330. <https://proceedings.mlr.press/v70/guo17a.html>
- Györfi, L., Kohler, M., Krzyzak, A., Walk, H., et al. 2002, *A distribution-free theory of nonparametric regression*, Vol. 1 (Springer)
- Hardle, W., Luckhaus, S., et al. 1984, Uniform consistency of a class of regression function estimators, *The Annals of Statistics*, 12, 612
- Ho, J., Jain, A., & Abbeel, P. 2020, Denoising Diffusion Probabilistic Models, *CoRR*, abs/2006.11239
- Ho, J., & Salimans, T. 2022, Classifier-Free Diffusion Guidance, *CoRR*, abs/2207.12598, doi: [10.48550/arXiv.2207.12598](https://doi.org/10.48550/arXiv.2207.12598)
- Hoogetboom, E., Gritsenko, A. A., Bastings, J., et al. 2021, Autoregressive Diffusion Models, *arXiv e-prints*, arXiv:2110.02037, doi: [10.48550/arXiv.2110.02037](https://doi.org/10.48550/arXiv.2110.02037)
- Ivezić, Ž., Kahn, S. M., Tyson, J. A., et al. 2019, LSST: From Science Drivers to Reference Design and Anticipated Data Products, *ApJ*, 873, 111, doi: [10.3847/1538-4357/ab042c](https://doi.org/10.3847/1538-4357/ab042c)
- Izbicki, R., & Lee, A. B. 2016, Nonparametric conditional density estimation in a high-dimensional regression setting, *Journal of Computational and Graphical Statistics*, 25, 1297
- . 2017, Converting high-dimensional regression to high-dimensional conditional density estimation, *Electronic Journal of Statistics*, 11, 2800
- Izbicki, R., Lee, A. B., & Pospisil, T. 2019, ABC–CDE: Toward Approximate Bayesian Computation With Complex High-Dimensional Data and Limited Simulations, *Journal of Computational and Graphical Statistics*, 1, doi: [10.1080/10618600.2018.1546594](https://doi.org/10.1080/10618600.2018.1546594)
- Izbicki, R., Shimizu, G., & Stern, R. 2020, in *International Conference on Artificial Intelligence and Statistics*, PMLR, 3068–3077
- Izbicki, R., Shimizu, G., & Stern, R. B. 2022, CD-split and HPD-split: Efficient Conformal Regions in High Dimensions, *Journal of Machine Learning Research*, 23, 1. <http://jmlr.org/papers/v23/20-797.html>
- Janowiak, J., Joyce, B., & Xie, P. 2020, NCEP/CPC L3 half hourly 4km global (60S - 60N) merged IR v1



- Jitkrittum, W., Kanagawa, H., & Schölkopf, B. 2020a, in Proceedings of Machine Learning Research, Vol. 124, Proceedings of the Thirty-Sixth Conference on Uncertainty in Artificial Intelligence, UAI 2020, virtual online, August 3-6, 2020, ed. R. P. Adams & V. Gogate (AUAI Press), 221–230. <http://proceedings.mlr.press/v124/jitkrittum20a.html>
- Jitkrittum, W., Kanagawa, H., & Schölkopf, B. 2020b, in Proceedings of Machine Learning Research, Vol. 124, Proceedings of the 36th Conference on Uncertainty in Artificial Intelligence (UAI), ed. J. Peters & D. Sontag (PMLR), 221–230. <http://proceedings.mlr.press/v124/jitkrittum20a.html>
- Jones, C., & Pewsey, A. 2019, The sinh-arcsinh normal distribution, Wiley Online Library
- Jones, M. C., & Pewsey, A. 2009, Sinh-arcsinh distributions, *Biometrika*, 96, 761
- Kingma, D. P., & Welling, M. 2013, Auto-Encoding Variational Bayes, arXiv e-prints, arXiv:1312.6114, doi: [10.48550/arXiv.1312.6114](https://doi.org/10.48550/arXiv.1312.6114)
- Kleinberg, J., Mullainathan, S., & Raghavan, M. 2016, Inherent trade-offs in the fair determination of risk scores, arXiv preprint arXiv:1609.05807
- Kobyzev, I., Prince, S. J. D., & Brubaker, M. A. 2021, Normalizing Flows: An Introduction and Review of Current Methods, *IEEE Trans. Pattern Anal. Mach. Intell.*, 43, 3964, doi: [10.1109/TPAMI.2020.2992934](https://doi.org/10.1109/TPAMI.2020.2992934)
- Kodra, D., Andrews, B. H., Newman, J. A., et al. 2023, Optimized Photometric Redshifts for the Cosmic Assembly Near-infrared Deep Extragalactic Legacy Survey (CANDELS), *ApJ*, 942, 36, doi: [10.3847/1538-4357/ac9f12](https://doi.org/10.3847/1538-4357/ac9f12)
- Koenker, R., & Bassett Jr., G. 1978, Regression quantiles, *Econometrica: Journal of the Econometric Society*, 33
- Koenker, R., & Hallock, K. F. 2001, Quantile regression, *Journal of Economic Perspectives*, 15, 143
- Kolouri, S., Park, S. R., Thorpe, M., Slepcev, D., & Rohde, G. K. 2017, Optimal mass transport: Signal processing and machine-learning applications, *IEEE signal processing magazine*, 34, 43
- Kuleshov, V., Fenner, N., & Ermon, S. 2018, in International conference on machine learning, PMLR, 2796–2804
- Kull, M., Perelló-Nieto, M., Kängsepp, M., et al. 2019, Beyond temperature scaling: Obtaining well-calibrated multiclass probabilities with Dirichlet calibration, *CoRR*, abs/1910.12656
- Kullback, S., & Leibler, R. A. 1951, On Information and Sufficiency, *The Annals of Mathematical Statistics*, 22, 79, doi: [10.1214/aoms/1177729694](https://doi.org/10.1214/aoms/1177729694)
- Lakshminarayanan, B., Pritzel, A., & Blundell, C. 2017, Simple and scalable predictive uncertainty estimation using deep ensembles, *Advances in neural information processing systems*, 30
- Laureijs, R., Amiaux, J., Arduini, S., et al. 2011, Euclid Definition Study Report, arXiv e-prints, arXiv:1110.3193, doi: [10.48550/arXiv.1110.3193](https://doi.org/10.48550/arXiv.1110.3193)

- Lei, J., G'Sell, M., Rinaldo, A., Tibshirani, R. J., & Wasserman, L. 2018, Distribution-free predictive inference for regression, *Journal of the American Statistical Association*, 113, 1094
- Leistedt, B., & Hogg, D. W. 2017, Data-driven, Interpretable Photometric Redshifts Trained on Heterogeneous and Unrepresentative Data, *ApJ*, 838, 5, doi: [10.3847/1538-4357/aa6332](https://doi.org/10.3847/1538-4357/aa6332)
- Li, L., Carver, R., Lopez-Gomez, I., Sha, F., & Anderson, J. 2024, Generative emulation of weather forecast ensembles with diffusion models, *Science Advances*, 10, eadk4489, doi: [10.1126/sciadv.adk4489](https://doi.org/10.1126/sciadv.adk4489)
- Liero, H. 1989, Strong uniform consistency of nonparametric regression function estimates, *Probability theory and related fields*, 82, 587
- Lim, B., Arik, S. Ö., Loeff, N., & Pfister, T. 2021, Temporal fusion transformers for interpretable multi-horizon time series forecasting, *International Journal of Forecasting*, 37, 1748
- Linhart, J., Gramfort, A., & Rodrigues, P. 2024, L-c2st: Local diagnostics for posterior approximations in simulation-based inference, *Advances in Neural Information Processing Systems*, 36
- Linhart, J., Gramfort, A., & Rodrigues, P. L. 2022, Validation Diagnostics for SBI algorithms based on Normalizing Flows, *arXiv preprint arXiv:2211.09602*
- Liu, Y., & Wu, Y. 2011, Simultaneous multiple non-crossing quantile regression estimation using kernel constraints, *Journal of Nonparametric Statistics*, 23, 415, doi: [10.1080/10485252.2010.537336](https://doi.org/10.1080/10485252.2010.537336)
- Lueckmann, J.-M., Goncalves, P. J., Bassetto, G., et al. 2017, Flexible statistical inference for mechanistic models of neural dynamics, *Advances in neural information processing systems*, 30
- Luo, R., Bhatnagar, A., Wang, H., et al. 2021, Localized Calibration: Metrics and Recalibration, *CoRR*, abs/2102.10809
- Malz, A. I., & Hogg, D. W. 2022, How to Obtain the Redshift Distribution from Probabilistic Redshift Estimates, *ApJ*, 928, 127, doi: [10.3847/1538-4357/ac062f](https://doi.org/10.3847/1538-4357/ac062f)
- Mandelbaum, R. 2018, Weak Lensing for Precision Cosmology, *Annual Review of Astronomy and Astrophysics*, 56, 393, doi: <https://doi.org/10.1146/annurev-astro-081817-051928>
- Mandelbaum, R., Seljak, U., Hirata, C. M., et al. 2008, Precision photometric redshift calibration for galaxy-galaxy weak lensing, *MNRAS*, 386, 781, doi: [10.1111/j.1365-2966.2008.12947.x](https://doi.org/10.1111/j.1365-2966.2008.12947.x)
- Marin, J.-M., Pudlo, P., Robert, C. P., & Ryder, R. J. 2012, Approximate Bayesian computational methods, *Statistics and computing*, 22, 1167
- Masserano, L., Dorigo, T., Izbicki, R., Kuusela, M., & Lee, A. B. 2022, Simulation-Based Inference with WALDO: Perfectly Calibrated Confidence Regions Using Any Prediction or Posterior Estimation Algorithm, *arXiv preprint arXiv:2205.15680*

- Matheson, J. E., & Winkler, R. L. 1976, Scoring rules for continuous probability distributions, *Management science*, 22, 1087
- McNeely, T., Khokhlov, P., Dalmasso, N., Wood, K. M., & Lee, A. B. 2023, Structural forecasting for short-term tropical cyclone intensity guidance, *Weather and Forecasting*
- McNeely, T., Vincent, G., Lee, A. B., Izbicki, R., & Wood, K. M. 2022, Detecting Distributional Differences in Labeled Sequence Data with Application to Tropical Cyclone Satellite Imagery, *arXiv preprint arXiv:2202.02253*
- Mirza, M., & Osindero, S. 2014, Conditional Generative Adversarial Nets, *CoRR*, abs/1411.1784
- Moreira, M. J. 2003, A conditional likelihood ratio test for structural models, *Econometrica*, 71, 1027
- Nichol, A. Q., & Dhariwal, P. 2021, in *Proceedings of Machine Learning Research*, Vol. 139, *Proceedings of the 38th International Conference on Machine Learning, ICML 2021, 18-24 July 2021, Virtual Event*, ed. M. Meila & T. Zhang (PMLR), 8162–8171. <http://proceedings.mlr.press/v139/nichol21a.html>
- Olander, T., Wimmers, A., Velden, C., & Kossin, J. P. 2021, Investigation of Machine Learning Using Satellite-Based Advanced Dvorak Technique Analysis Parameters to Estimate Tropical Cyclone Intensity, *Weather and Forecasting*, 36, 2161
- Papamakarios, G., & Murray, I. 2016, Fast  $\epsilon$ -free inference of simulation models with bayesian conditional density estimation, *Advances in neural information processing systems*, 29
- Papamakarios, G., Nalisnick, E., Jimenez Rezende, D., Mohamed, S., & Lakshminarayanan, B. 2019, Normalizing Flows for Probabilistic Modeling and Inference, *arXiv e-prints*, arXiv:1912.02762. <https://arxiv.org/abs/1912.02762>
- Papamakarios, G., Nalisnick, E., Rezende, D. J., Mohamed, S., & Lakshminarayanan, B. 2019, Normalizing Flows for Probabilistic Modeling and Inference. <https://arxiv.org/abs/1912.02762>
- Radford, A., Wu, J., Child, R., et al. 2019, Language Models are Unsupervised Multitask Learners
- Rahaman, R., et al. 2021, Uncertainty quantification and deep ensembles, *Advances in Neural Information Processing Systems*, 34, 20063
- Ravuri, S., Lenc, K., Willson, M., et al. 2021, Skilful precipitation nowcasting using deep generative models of radar, *Nature*, 597, 672, doi: [10.1038/s41586-021-03854-z](https://doi.org/10.1038/s41586-021-03854-z)
- Robert, C. P., Casella, G., & Casella, G. 1999, *Monte Carlo statistical methods*, Vol. 2 (Springer)
- Romano, Y., Patterson, E., & Candès, E. 2019, in *Advances in Neural Information Processing Systems*, Vol. 32 (Curran Associates, Inc.), 3543–3553
- Sadeh, I., Abdalla, F. B., & Lahav, O. 2016, ANNz2: Photometric Redshift and Probability Distribution Function Estimation using Machine Learning, *PASP*, 128, 104502, doi: [10.1088/1538-3873/128/968/104502](https://doi.org/10.1088/1538-3873/128/968/104502)

- Santambrogio, F. 2015, Optimal transport for applied mathematicians, Birkäuser, NY, 55, 94
- Schmidt, S. J., Malz, A. I., Soo, J. Y. H., et al. 2020, Evaluation of probabilistic photometric redshift estimation approaches for The Rubin Observatory Legacy Survey of Space and Time (LSST), MNRAS, 499, 1587, doi: [10.1093/mnras/staa2799](https://doi.org/10.1093/mnras/staa2799)
- Schmit, T. J., Griffith, P., Gunshor, M. M., et al. 2017, A closer look at the ABI on the GOES-R series, Bulletin of the American Meteorological Society, 98, 681
- Sisson, S. A., Fan, Y., & Beaumont, M. 2018, Handbook of approximate Bayesian computation (CRC Press)
- Sohl-Dickstein, J., Weiss, E. A., Maheswaranathan, N., & Ganguli, S. 2015, Deep Unsupervised Learning using Nonequilibrium Thermodynamics, CoRR, abs/1503.03585
- Stute, W., & Zhu, L. X. 2002, Model checks for generalized linear models, Scandinavian Journal of Statistics, 29, 535
- Tagasovska, N., & Lopez-Paz, D. 2019, in Advances in Neural Information Processing Systems 32: Annual Conference on Neural Information Processing Systems 2019, NeurIPS 2019, December 8-14, 2019, Vancouver, BC, Canada, ed. H. M. Wallach, H. Larochelle, A. Beygelzimer, F. d’Alché-Buc, E. B. Fox, & R. Garnett, 6414–6425. <https://proceedings.neurips.cc/paper/2019/hash/73c03186765e199c116224b68adc5fa0-Abstract.html>
- Talts, S., Betancourt, M., Simpson, D., Vehtari, A., & Gelman, A. 2018, Validating Bayesian inference algorithms with simulation-based calibration, arXiv preprint arXiv:1804.06788
- Taylor, J. W., & Bunn, D. W. 1999, A quantile regression approach to generating prediction intervals, Management Science, 45, 225
- The LSST Dark Energy Science Collaboration, Mandelbaum, R., Eifler, T., et al. 2018, The LSST Dark Energy Science Collaboration (DESC) Science Requirements Document, arXiv e-prints, arXiv:1809.01669, doi: [10.48550/arXiv.1809.01669](https://doi.org/10.48550/arXiv.1809.01669)
- Timmermann, A. 2000, Density forecasting in economics and finance, Journal of Forecasting, 19, 231
- van den Oord, A., & Kalchbrenner, N. 2016, Pixel RNN
- Van den Oord, A., Kalchbrenner, N., Espeholt, L., et al. 2016, Conditional image generation with pixelcnn decoders, Advances in neural information processing systems, 29
- Vaswani, A., Shazeer, N., Parmar, N., et al. 2017, in Advances in Neural Information Processing Systems 30: Annual Conference on Neural Information Processing Systems 2017, December 4-9, 2017, Long Beach, CA, USA, ed. I. Guyon, U. von Luxburg, S. Bengio, H. M. Wallach, R. Fergus, S. V. N. Vishwanathan, & R. Garnett, 5998–6008. <https://proceedings.neurips.cc/paper/2017/hash/3f5ee243547dee91fbd053c1c4a845aa-Abstract.html>

- Villani, C. 2021, Topics in optimal transportation, Vol. 58 (American Mathematical Soc.)
- Vovk, V., Gammerman, A., & Shafer, G. 2005, Algorithmic Learning in a Random World (Springer Science & Business Media)
- Wald, Y., & Globerson, A. 2017, in Advances in Neural Information Processing Systems 30: Annual Conference on Neural Information Processing Systems 2017, December 4-9, 2017, Long Beach, CA, USA, ed. I. Guyon, U. von Luxburg, S. Bengio, H. M. Wallach, R. Fergus, S. V. N. Vishwanathan, & R. Garnett, 6359–6368. <https://proceedings.neurips.cc/paper/2017/hash/3eb414bf1c2a66a09c185d60553417b8-Abstract.html>
- Wehenkel, A., & Louppe, G. 2019, in Advances in Neural Information Processing Systems 32: Annual Conference on Neural Information Processing Systems 2019, NeurIPS 2019, December 8-14, 2019, Vancouver, BC, Canada, ed. H. M. Wallach, H. Larochelle, A. Beygelzimer, F. d’Alché-Buc, E. B. Fox, & R. Garnett, 1543–1553. <https://proceedings.neurips.cc/paper/2019/hash/2a084e55c87b1ebcdaad1f62fdbbac8e-Abstract.html>
- York, D. G., Adelman, J., Anderson, John E., J., et al. 2000, The Sloan Digital Sky Survey: Technical Summary, AJ, 120, 1579, doi: [10.1086/301513](https://doi.org/10.1086/301513)
- Zhao, D., Dalmaso, N., Izbicki, R., & Lee, A. B. 2021, in Proceedings of Machine Learning Research, Vol. 161, Proceedings of the Thirty-Seventh Conference on Uncertainty in Artificial Intelligence, ed. C. de Campos & M. H. Maathuis (PMLR), 1830–1840. <https://proceedings.mlr.press/v161/zhao21b.html>
- Zhao, S., Ma, T., & Ermon, S. 2020, in International Conference on Machine Learning, PMLR, 11387–11397
- Zhou, R., Newman, J. A., Mao, Y.-Y., et al. 2021, The clustering of DESI-like luminous red galaxies using photometric redshifts, MNRAS, 501, 3309, doi: [10.1093/mnras/staa3764](https://doi.org/10.1093/mnras/staa3764)